minerals

Article

Geochemical Characteristics of the Mineral Assemblages from the Niukutou Pb-Zn Skarn Deposit, East Kunlun Mountains, and Their Metallogenic Implications

Xinyu Wang, Shulai Wang, Huiqiong Zhang *, Yuwang Wang, Xinyou Zhu and Xing Yang

Beijing Institute of Geology for Mineral Resources Co., Ltd., Beijing 100012, China
* Correspondence: zhqzhq_2005@163.com; Tel.: +86-010-8492-9180

Abstract: The Niukutou Pb-Zn deposit is typical of skarn deposits in the Qimantagh metallogenic belt (QMB) in the East Kunlun Mountains. In this study, based on detailed petrographical observations, electron microprobe analyses (EMPAs), and laser-ablation–inductively coupled plasma–mass spectrometry (LA-ICP-MS) analyses, we report the major and trace element compositions of the typical skarn mineral assemblages (garnet, pyroxene, ilvaite, epidote, and chlorite) in this deposit. Three hydrothermal mineralization stages with different mineral assemblages of the prograde metamorphic phase were determined, which were distributed from the inside to the outside of the ore-forming rock mass. Grt1+Px1 (Stage 1), Grt2+Px2 (Stage 2), and Px3 (Stage 3) were distinguished in the Niukutou deposit. Furthermore, the ilvaites in the retrograde metamorphic phase can be divided into three stages, namely Ilv1, Ilv2, and Ilv3. The ore-forming fluid in Stage 1 exhibited high $\sum$REE, U, and Nd concentrations and δEu, δCe, and LREE/HREE values, which were likely derived from a magmatic–hydrothermal source and formed at high temperatures, high fO_2 values, and mildly acidic pH conditions, and probably experienced diffusive metasomatism in a closed system with low water/rock ratios. In Stages 2 and 3, the ore-forming exhibited lower $\sum$REE, U, and Nd concentrations and δEu, δCe, and LREE/HREE values, with high Mn content that had likely experienced infiltrative metasomatism in an open system with high water/rock ratios. From Ilv1 to Ilv3, the δEu and U contents decreased, whereas the Mn content increased, indicating that the oxygen fugacity of mineralization was in decline. The ore-forming fluid evolution of the Niukutou deposit can be characterized as follows: from Stage 1 to Stage 3, the hydrothermal fluid migrated from the deep plutons to the shallow skarn and marble; the environment altered from the high fO_2 and temperature conditions to low fO_2 and temperature values, and the pH and Mn contents increased. The fluids contained considerable metal ore-forming materials that were favorable for the enrichment and precipitation of the Fe content. In the retrograde metamorphic phase, with the decrease in oxygen fugacity (from Ilv1 to Ilv3), the temperature and oxygen fugacity of the theore-forming fluid environment decreased, ultimately becoming conducive to the dissolution and precipitation of Pb and Zn elements.

Keywords: mineralogical characteristics; geochemistry; metallogenic process; Niukutou skarn Pb-Zn deposit; East Kunlun Mountains

1. Introduction

The Qimantagh metallogenic belt (QMB) is a significant Fe-Pb-Zn-Cu (-Ag) mineral belt that extends for 550 km in the East Kunlun Mountains, on the northern Tibetan Plateau (Figure 1a; [1–7]). Skarn deposits in the QMB can be subdivided into several main types based on the dominant metal. Typical Cu (Mo) skarn deposits are found in Kaerqueka, Wulanwuzhuer, and Yazigou (Figure 1b); Fe skarn deposits occur in Yemaquan, Galinge, and Kendekeke, whereas Pb-Zn skarn deposits are found in Weibao, Sijiaoyang, and Niukutou. Furthermore, small deposits and mines are scattered throughout the region, a fact that has attracted the attention of many researchers [7–11]. Published studies

have shown that the skarn mineralization in this area is genetically related to Triassic granitoids [12,13] and that different deposits are generally characterized by a distinct skarn mineral composition. However, the feature(s) of the ore-forming fluids that control the mineralization types in the QMB remain unclear, limiting our understanding of the skarn mineralization mechanisms in the region.
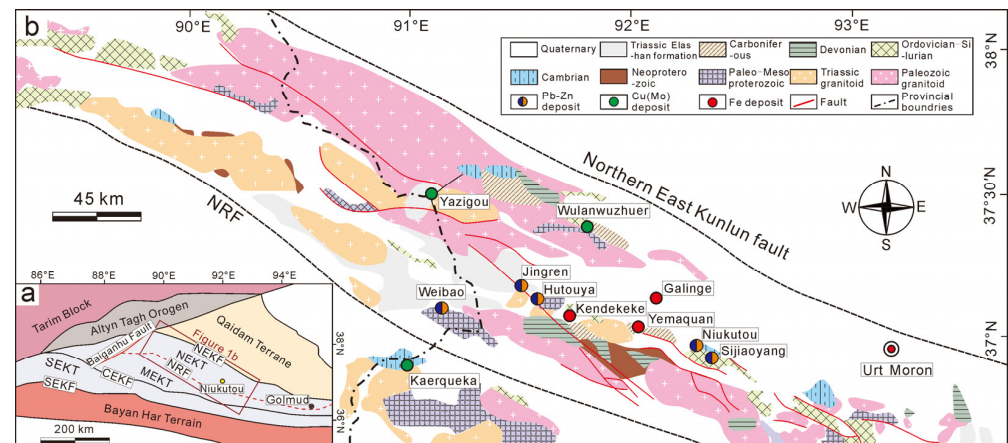
Figure 1. Tectonic framework of the eastern Kunlun area (**a**) and regional geological and mineral map of the Niukutou deposit (**b**) (modified from [2,12,13]). Abbreviations: NEKT—Northeast Kunlun terrane; NEKF—Northeast Kunlun fault; NRF—Nalingguole River fault; CEKF—Central-East Kunlun fault; MEKT—Middle-East Kunlun terrane; SEKT—Southeast Kunlun terrane; and SEKF—Southeast Kunlun fault.

The Niukutou Pb-Zn skarn deposit is located in the eastern part of the QMB (Figure 1b). Skarn minerals are strongly developed within the Niukutou deposit, and the deposit's geological structure, zonation pattern, and mineral assemblages have been described [14–17]. However, the detailed mineralogical characteristics and chemistry of the skarn minerals, as well as their implications, have not been examined, hence restricting any discussion of the metalogic geological conditions and regularity of the Niukutou deposit. Skarn minerals, especially those that preserve complex chemical zonation patterns, can record the composition and evolutionary history of hydrothermal processes. Furthermore, through the application of analytical techniques, including electron microprobe analysis (EMPA) and laser-ablation–inductively coupled plasma–mass spectrometry (LA-ICP-MS), hydrothermally altered minerals have been successfully used as an important probe for researching the environment of the metal accumulation, prospecting, and evolution of ore-forming fluids within ore deposits [18–20].

In this paper, we present the mineralogical characteristics and petrographic features representing the three ore-forming stages, as well as the major and trace element chemical data, for the mineral assemblages in the Niukutou deposit. We discuss the ore-forming conditions and evolution of the ore-forming fluids within the deposit, with the ultimate aim of revealing the processes that underlie the metal ore-forming mechanism and developing a superior understanding of the implications for the Niukutou mineralization.

2. Regional Geology

The Qimantagh area is wedged among the Altyn Tagh Orogen, Qaidam Basin, and Bayan Har terrain and bounded by the Altyn Tagh Fault, the Northern Kunlun Fault, and the Nalingguole River Fault (Figure 1a). Igneous rocks of different ages ranging from the Archean to the Cenozoic occur widely within the Qimantagh area (Figure 1b). The Langyashan Formation, Tanjianshan Group, and Carboniferous strata are the most important host rocks for skarn mineralization within the Qimantagh area [6,7,12,21]. The Mesoproterozoic Langyashan Formation consists of carbonate and clastic rocks locally undergoing greenschist-facies metamorphism [7]. The Ordovician–Silurian Tanjianshan

Group consists of volcano-sedimentary rocks that have also experienced greenschist-facies metamorphism.

Faults in this region generally strike in the NWW and NW directions and are interpreted to have developed before or during skarn alteration, thus usually controlling significant mineralization. The NE- and N-striking fault systems are generally postdated skarns and mineralization [22]. The fold orientations mostly trend from the NWW to the SN. Intrusive rocks formed in the Hercynian and Indosinian periods and were controlled by NW- and NWW-oriented faults. Schistosity and cleavage are common in these rocks.

3. Deposit Geology

The Niukutou Pb-Zn skarn deposit is located in the eastern part of the QMB (Figure 1b) and comprises three ore blocks (or magnetic anomalies) referred to as M1, M4, and M2, from west to east. The Pb-Zn mineralization crops out within the M1 and M4 ore blocks (Figure 2), with the resources being more than 1.14 million tons.
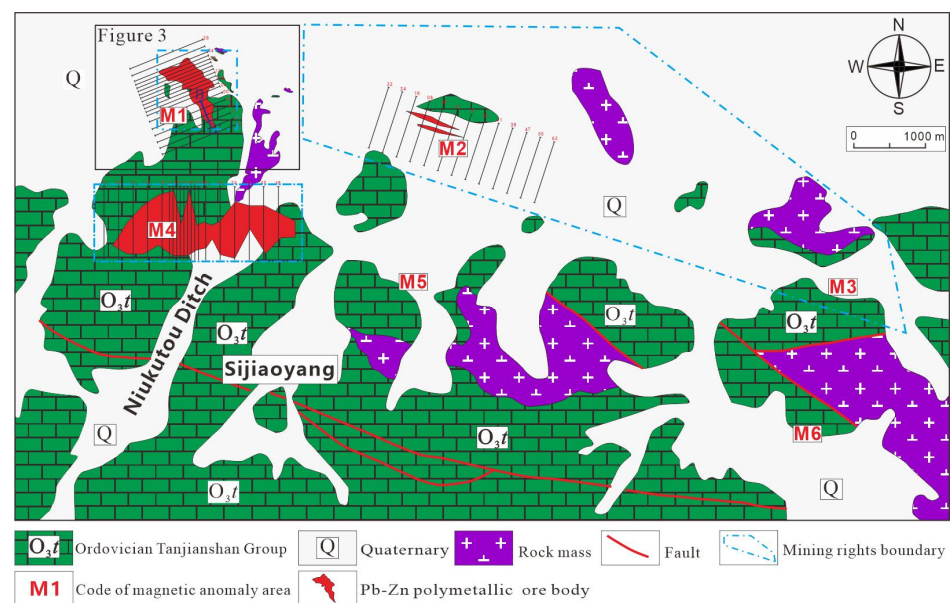
Figure 2. Simplified geological map of the Niukutou Pb-Zn polymetal deposit showing the locations of the M1, M4, and M2 ore blocks.

The Tanjianshan Group and Quaternary deposits are the main sedimentary formations. The Tanjianshan Group is primarily composed of limestone, banded limestone, and marble, representing a set of shallow marine carbonate deposits. Similar to the Hutouya skarn Cu-Pb-Zn deposit, the Tanjianshan Group is the host for the skarn ore bodies in the Niukutou deposit. Where this group contacts with the Triassic granitoids, limestone becomes calc-silicate hornfels with well-developed skarn zonation.

Granodiorite and monzonitic granite are the main intrusive rocks in the M1 and M4 ore blocks (Figure 3). The granodiorite is closely related to Pb-Zn mineralization. The age of the ore-forming-related granites is 375.4 ± 4.6 Ma [5]. The granodiorite occurs both on the surface and at the bottoms of drill holes, and the monzonitic granite occurs only in the M2 ore block.

The ore bodies in the M1 and M4 ore blocks primarily occur in layered skarns (Figure 4a), and most Pb-Zn ore minerals are hosted in johannsenite, ilvaite, and mangan–hedenbergite skarns (Figure 4b). The main ore textures are heterogeneous granular and columnar. The ore structures are dominated by banded, densely disseminated, and massive patterns. The ore minerals include galena, sphalerite, pyrrhotite, magnetite, pyrite, arsenopyrite, bornite, and chalcopyrite. The main skarn minerals are garnet, johannsenite, ilvaite, mangan–hedenbergite, actinolite, tremolite, quartz, calcite, and chlorite.
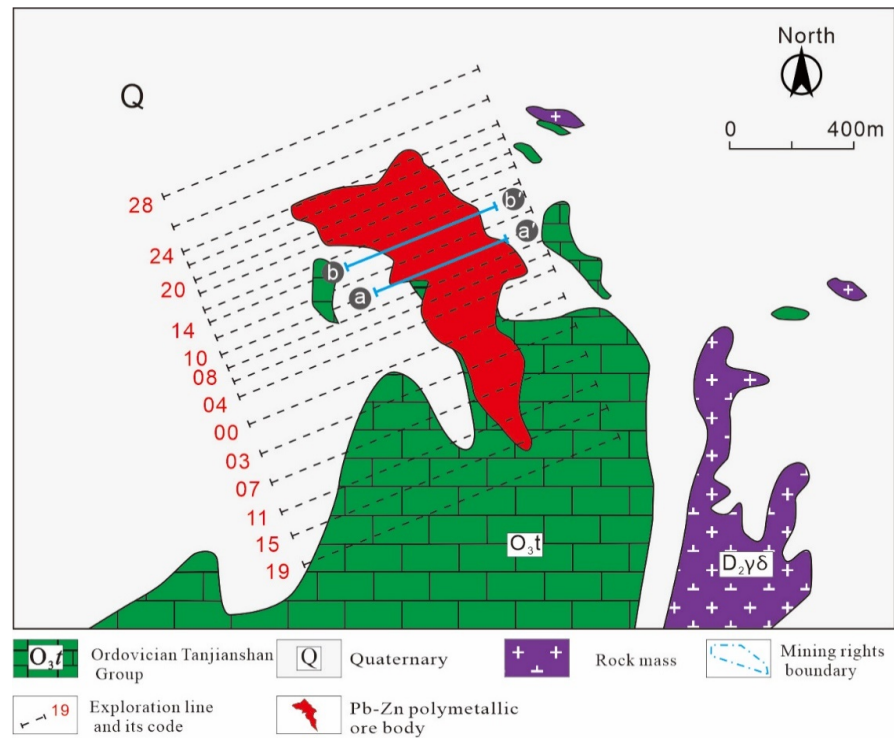
Figure 3. Geological map of the Niukutou M1 ore block.
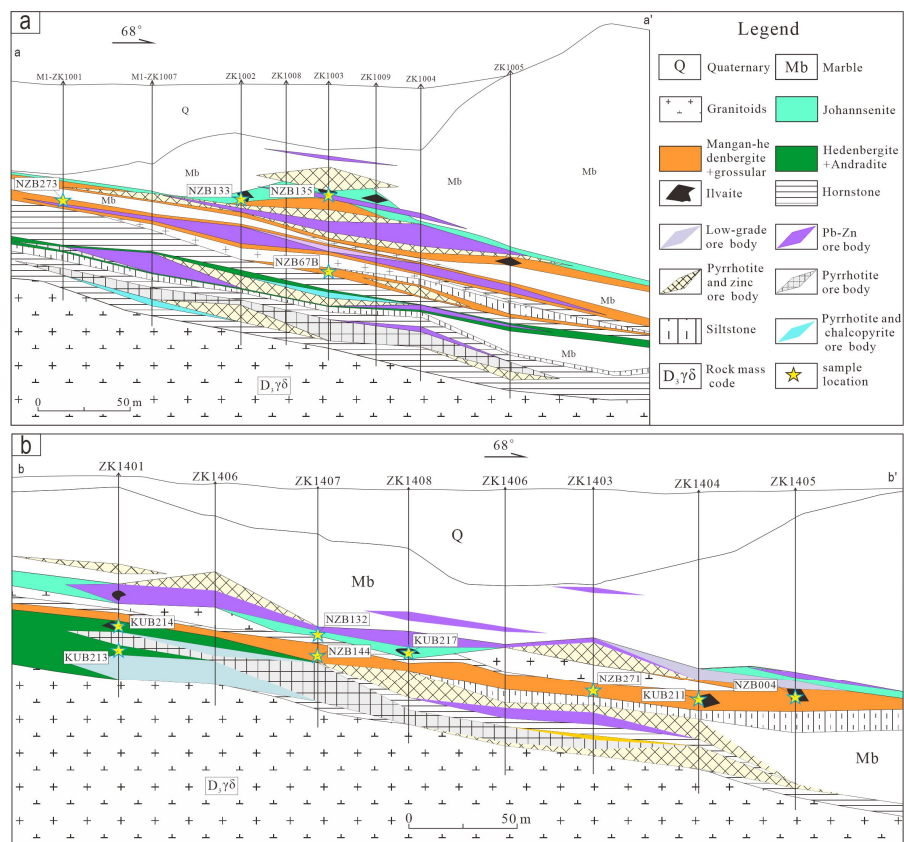
Figure 4. Geological profile of the No. 10 (**a**) and No. 14 (**b**) exploration lines in the M1 ore block of the Niukutou deposit.

Based on the mineral assemblages, ore textures, and crosscutting relationships, the skarn formation and mineralization of the Niukutou deposit can be divided into four phases (Figure 5): (1) in the prograde metamorphic phase, the main mineral assemblages consist of anhydrous minerals such as garnet and pyroxene; (2) in the retrograde metamorphic phase, the main mineral assemblage is dominated by hydrous silicate minerals, characteristically ilvaite, actinolite, tremolite, epidote, and chlorite, which often replace prograde garnet/pyroxene; (3) the sulfide phase is the main ore-forming phase, where the mineral assemblage consists of ore minerals such as pyrrhotite, pyrite, sphalerite, galena, and quartz; and (4) in the carbonate phase, the mineral assemblage is characterized by quartz and calcite veins that cut through the skarn and ore minerals.

Minerals \ Phases	Prograde phase	Retrograde phase	Sulfide phase	Carbonate phase
Garnet	▬▬▬			
Pyroxene	▬▬▬			
Ilvaite		———		
Tremolite		– – –		
Actinolite		– – –		
Magnetite		———	– – –	
Quartz		– – –	———	– – –
Galena		– – –	———	– – –
Sphalerite		– – –	▬▬▬	– – –
Pyrrhotite		– – –	▬▬▬	– – –
Chalcopyrite		– – –	———	– – –
Pyrite		– – –	———	– – –

Abundant ▬▬▬　　Local ———　　Trace – – –
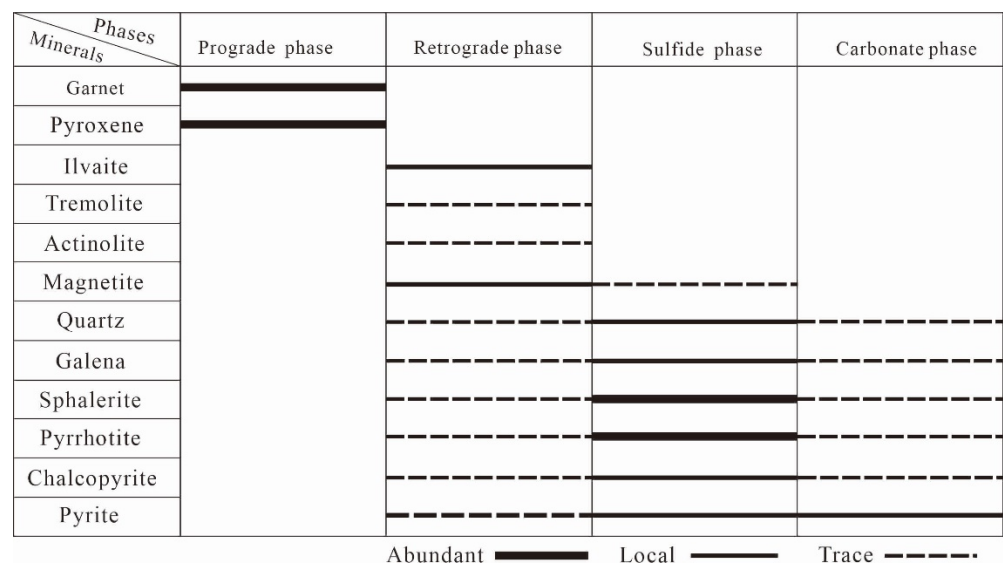
Figure 5. Division of mineralization sequence of the Niukutou skarn deposit.

According to their geological occurrence and mineral texture, the prograde garnets can be divided into two subtypes, Grt1 and Grt2, whereas the prograde pyroxenes can be divided into three subtypes, Px1, Px2, and Px3. The ilvaite in the late phase also has three subtypes, Ilv1, Ilv2, and Ilv3.

Grt1 is usually dark brown (Figure 6a,b), brownish green, or brown in color and is occasionally reddish brown. The crystal diameter is generally greater than 500 μm, with most being greater than 1000 μm. Grt1 often coexists with Px1 (Figure 6a), pyrrhotite (Figure 6b), and magnetite. Grt2 is light brown and brownish green (Figure 6c) with grain sizes of between 500 and 1000 μm; thus, the grain is smaller than in Grt1. Compared with Grt1, the crystal form of Grt2 is incomplete, indicating stronger alteration. Grt2 generally coexists with Px2 or is replaced with Ilv2 (Figure 6d).

Px1 is generally dark green in color and columnar to short columnar and granular in shape. It usually coexists or is replaced with Ilv1 or magnetite (Figure 6e). Px2 is light green (Figure 6f), columnar to short columnar in shape, and found in the M1 ore block and secondarily in the M4 ore block. Generally, it coexists or is replaced with Ilv2. Px2 is associated with pyrrhotite and galena.

Px3 is brown or dark brown in color, with fibrous and long-columnar types (Figure 6i). Px3 often coexists with Ilv3 and develops with sphalerite and galena. It is often cut through by calcite veins in the later stages.
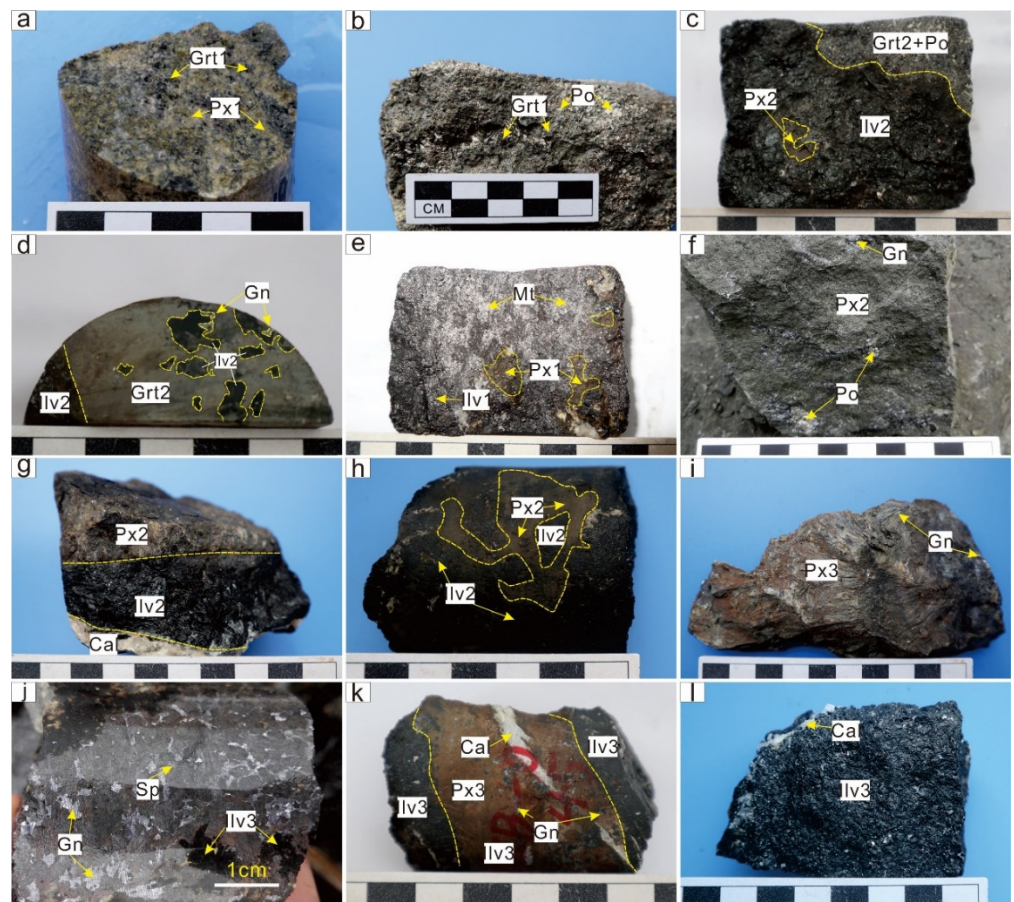
Figure 6. Photographs of representative samples and their relationships to the Niukutou deposit. (**a**) Granular garnet (Grt1) and hedenbergite (Px1) from the M1 pit; (**b**) Coarse-grained garnet (Grt1) replaced with pyrrhotite; (**c**) Granular garnet (Grt2) coexisting with Mn–hedenbergite (Px2), and short-column ilvaite (Ilv2) replaced the garnet (Grt2) and Mn–hedenbergite (Px2), whereas the Mn–hedenbergite (Px2) is residual in the ilvaite (Ilv2); (**d**) Fine-grained garnet (Grt2) is replaced with short-column Ilvaite (Ilv2); (**e**) Ilv1 is replaced with disseminated magnetite and the hedenbergite (Px1) is residual in the ilvaite (Ilv2); (**f**) Disseminated galena and pyrrhotite are developed in the short-column Mn-hedenbergite (Px2); (**g**) Mn–hedenbergite (Px2) is replaced with ilvaite (Ilv2), the ilvaite skarn is cut through by calcite veins; (**h**) Short-column ilvaite (Ilv2) replaced the Mn–hedenbergite (Px2); (**i**) Fibrous or long-column johannsenite (Px3), with minor disseminated galena; (**j**) Galena and sphalerite are developed between the ilvaite (Ilv3) grains; (**k**) Ilvaite (Ilv3) replaced johannsenite (Px3), with minor disseminated galena developed in it and cut by calcite veins; (**l**) The short-column ilvaite (Ilv3) cut by calcite veins. Abbreviations: Grt1, Px1, Ilv1—Garnet, pyroxene, and ilvaite of Stage 1; Grt2, Px2, Ilv2—Garnet, pyroxene, and ilvaite of Stage 2; Px3, Ilv3—Pyroxene and ilvaite of Stage 2; Gn—Galena; Sp—Sphalerite; Po—Pyrrhotite; Mt—Magnetite; Cal—Calcite.

Based on the mineral assemblages and microscopic characteristics, there are three ilvaite-bearing mineral assemblages in the Niukutou deposit (unpublished data): (1) Ilv1 replaced Grt1, Px1, and magnetite (Figure 6e); (2) Ilv2 replaced Grt2, Px2, galena, and magnetite (Figure 6g,h); and (3) Ilv3 replaced Px3 (johannsenite; Figure 6j,k) and is often cut through by calcite and quartz veins (Figure 6l). Grt1 and Px1 are generated in Stage 1 of the prograde metamorphic phase, whereas Grt2/Px2 and Px3 are generated in Stage 2 of the prograde metamorphic phase. Ilv1 to Ilv3 are generated in three different stages of the retrograde metamorphic phase.

4. Mineralogical Characteristics

4.1. Analytical Methods

A total of 36 representative samples from the Niukutou deposit were examined in this study; parts of the sample location are shown in Figure 4. Most samples were collected from the mining pit and drill cores. The paragenetic relationships were studied in thin sections by transmitted polarized light microscopy and in polished thick sections by reflected light microscopy. To further determine the mineralogical characteristics of the Niukutou skarn deposit, we selected skarn and ore minerals in each phase for EMPA analysis. The EMPA analysis and test work were performed at the Institute of Geology, Chinese Academy of Geosciences. The instrument used was a JXA-8100 system (JEOL Company, Tokyo, Japan). The analytical parameters were as follows: accelerating voltage 15 k, beam current 2×10^{-8} A, spectral time 10 s, beam size 5 μm, ZAF correction, and SPI-combined standard sample correction.

The cation numbers and end tuples of the garnet, pyroxene, and amphibole minerals were calculated using Geokit software (GeokitPro20221030) [23], and the cation numbers of epidote and chlorite were calculated using CalcMin software [24].

To obtain the trace elements of the skarn samples, we chose representative skarn minerals (garnet, pyroxene, and ilvaite) and ground them into probe pieces (with thicknesses greater than 100 μm) for LA-ICP-MS analysis.

The laser-ablation system was an yttrium–aluminum garnet laser produced by the New Wave Company, Stockholm, Sweden), with a wavelength of 213 nm. The ICP-MS was performed with a Thermo Element II instrument (Agilent 7700a, NYSE: A, Palo Alto City, United States) (version, manufacturer, city, country). In the process of laser-ablation sampling, helium was used as the carrier gas. Before the helium carried the sample aerosol into the ICP, it was mixed with argon (carrier gas, plasma gas, and compensation gas) through a T-joint. To obtain the best signal strength and stability of standard NIST SRM 612, the experimental conditions were optimized by adjusting the helium and argon gas flows, and the oxide yields were controlled to be less than 0.3%. For unknown samples, the laser-sampling method was single-point erosion: the diameter of the beam spot was 40 μm; the frequency was 10 Hz; and the energy density was about 9 J/cm^2, with a 20 s gas blank +40 s sample erosion +20 s washing. The signal detection adopted low-resolution electric field scanning and peak-skipping acquisition, and the detection time for each element was 10 ms. Silicate, quartz, and other minerals were corrected with NIST SRM 610 and GSE-1G as the external standards, and the internal standard element was ^{29}Si; sulfide was corrected with NIST SRM 610 and mass-1 as the external standards.

4.2. Mineralogical Characteristics and Petrographic Features

As previously noted, the prograde garnet–pyroxene and retrograde ilvaite–epidote-chlorite assemblages are the dominant skarn minerals in the Niukutou deposit.

4.2.1. Garnet

Garnet is pervasive in the Niukutou deposit. According to the geological occurrence, microscopic characteristics, and composition, the Niukutou garnet can be divided into two subtypes (Figure 7).

Grt1 is automorphic or semi-automorphic. From the core to the rim, grains show clear growth zonation (Figure 7a–c). Additionally, Grt1 coexists with pyroxene (Px1) in the same stage (Figure 7a,b). It was generally metasomatized by retrograde ilvaite–chlorite–epidote and associated with the magnetite–pyrrhotite–sphalerite ore minerals.

Grt2 is distinguished from Grt1 by its unzoned character (Figure 7c,d). In terms of microscopic mineral texture, Grt2 is generally found around Grt1, suggesting that Grt1 crystallized earlier than Grt2. Some Grt2 exhibits a poor crystal form and develops with cracks (Figure 7e).
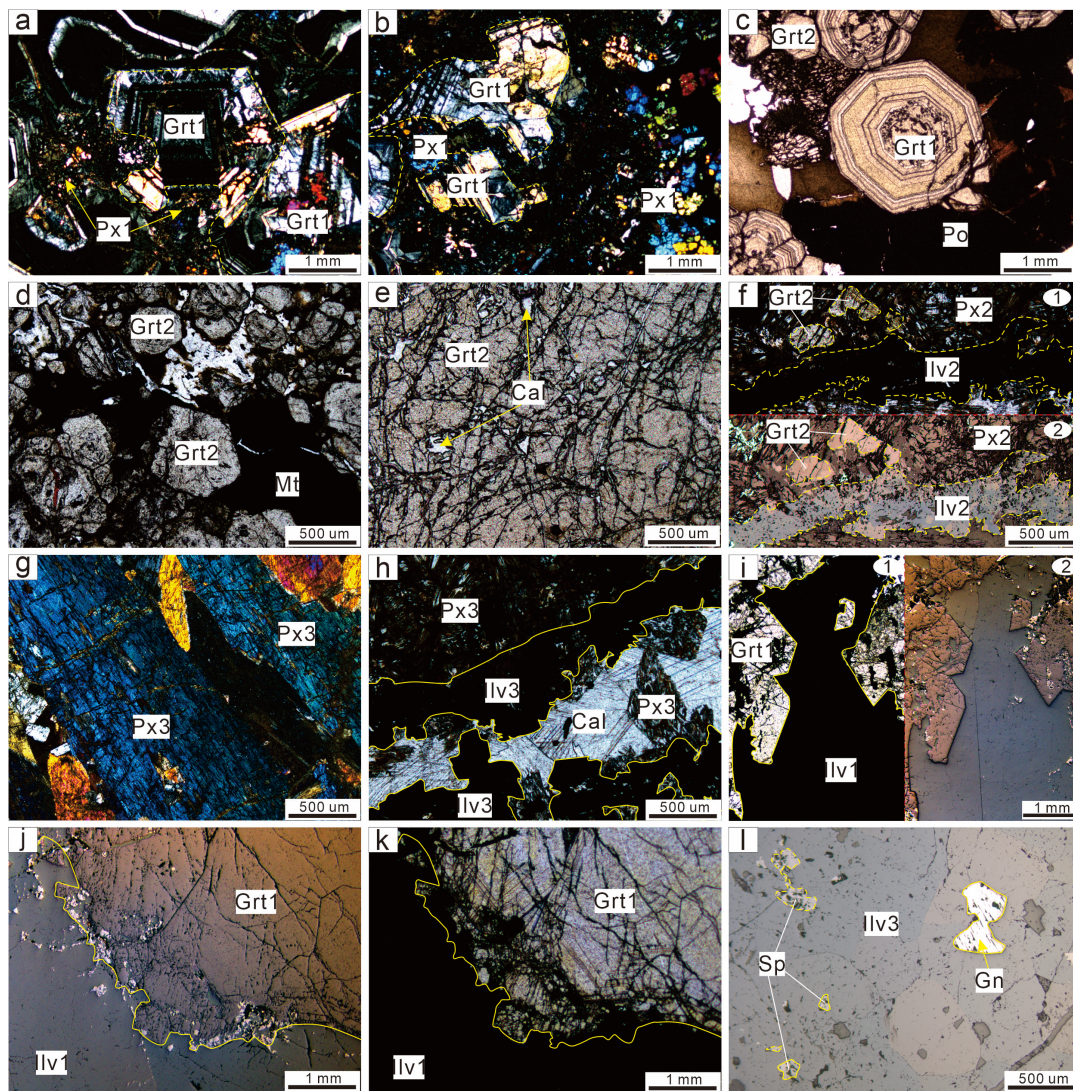
Figure 7. Photomicrographs of representative samples from different stages and their relationships in the Niukutou deposit. (**a**) Zoned garnet (Grt1) coexisting or replaced with hedenbergite (Px1) in cross-polarized light; (**b**) Zoned garnet (Grt1) coexisting or replaced with hedenbergite (Px1) in cross-polarized light; (**c**) Zoned garnet (Grt1) replaced with pyrrhotite, followed by the unzoned garnet (Grt2) in plane-polarized light; (**d**) Unzoned garnet (Grt2) replaced with magnetite (plane-polarized light); (**e**) Grt2 developed with cracks; (**f**) Grt2 and Px2 are replaced with Ilv2 (plane-polarized light in 1 and reflected light in 2); (**g**) Fibrous or long-column johannsenite (Px3) in cross-polarized light; (**h**) johannsenite (Px3) is replaced with ilvaite (Ilv3) and cut by a calcite vein (plane-polarized light); (**i**) Zoned garnet (Grt1) is replaced with the ilvaite (Ilv1, plane-polarized light in 1 and reflected light in 2); (**j**,**k**) Zoned garnet (Grt1) is replaced with Ilv1 (reflected light in j and plane-polarized light in k); (**l**) Disseminated galena and sphalerite developed within Ilv3 (reflected light). Abbreviations: Grt1, Px1, Ilv1—Garnet, pyroxene, and ilvaite of Stage 1; Grt2, Px2, Ilv2—Garnet, pyroxene, and ilvaite of Stage 2; Px3, Ilv3—Pyroxene and ilvaite of Stage 2; Gn—Galena; Sp—Sphalerite; Po—Pyrrhotite; Mt—Magnetite; Cal—Calcite.

4.2.2. Pyroxene

Pyroxene is also one of the main skarn minerals in the Niukutou deposit, and it normally occurs together with garnet; it was formed in the prograde stage.

According to the geological occurrence, microscopic metasomatic relationships, and EMPA composition, the pyroxene in the Niukutou deposit can also be divided into three types.

Under the microscope, Px1 is usually dark green in color and columnar to short columnar and granular in shape; it exhibits a high-grade yellow-green interference color and the typical cross joint of pyroxene (Figure 7a,b). It occurs mostly in the M1 ore block (in the deep part of the drill holes) and often coexists with Grt1 (Figure 7a,b).

In contrast, Px2 is short columnar or fibrous in shape and shows a graded yellow-green interference color (Figure 7f). Px2 coexists with Grt2 and is replaced with Ilv2 (Figure 7f).

Compared to Px2, Px3 is often distributed in the outer zone of the deposit. Px3 has a long-columnar shape and fibrous texture (Figure 7g,h) and shows a dark-green or grass-green color in plane-polarized light. Px3 is often replaced with Ilv3, develops with sphalerite and galena, and is associated with Pb-Zn mineralization.

4.2.3. Ilvaite

The typical ilvaite sample is black and shows a columnar or long-columnar shape. It shows a black or dark-brown color in plane-polarized light and a light-blue color in reflected light (Figure 7f,i,j). There are longitudinal grains on the cylinder measuring 3–10 mm on the long axis. It is soluble in hydrochloric acid and shows a white emulsion shape after dissolution. Quartz, sphalerite, and galena develop between the ilvaite grains and crevices. Calcite veins occasionally cut through the ilvaite. From microscopy, it is difficult to distinguish the three types of ilvaites. However, different mineral assemblages could differentiate the three types of ilvaites.

Ilv1 occasionally replaces Grt1 (Figure 7i–k). Pyrrhotite often develops between Ilv1 and Grt1.

Ilv2 replaces Grt2 and Px2 (Figure 7f). Sphalerite or galena often develops between Ilv1 and Grt1.

Ilv3 generally replaces Px3 (Figure 7h). Sp and Gn often develop within Ilv3 (Figure 7l) or in the contact zone between Ilv3 and Px3. Compared to Ilv2, the galena content of Ilv3 is higher. Additionally, calcite veins cut through or develop within Ilv3.

4.2.4. Epidote

Epidote shows granular to short-columnar structures. Under plane-polarized light, it is light straw yellow and is generally replaced with sphalerite. Under orthogonally polarized light, it has abnormal interference colors. It often replaces prograde garnet and pyroxene, indicating that epidote clearly formed later than the early skarn minerals.

4.2.5. Chlorite

Chlorite is common in the deposit, and we chose only two representative samples for the EMPA. Chlorite is generally replaced with prograde garnet–pyroxene. Under the microscope, chlorite has flake-, scale-, and rose-like shapes.

5. Results

5.1. Major Chemical Elements of Minerals

5.1.1. Garnet

The contents of the major elements and the calculated end-member compositions of the garnets are listed in Table S1. Electron microprobe analyses showed that the garnet crystals from the Nikutou deposit belonged to the andradite–grossular solid solutions and contained less pyralspite (sum of pyrope, spessartine, almandine, and uvarovite; Figure 8).
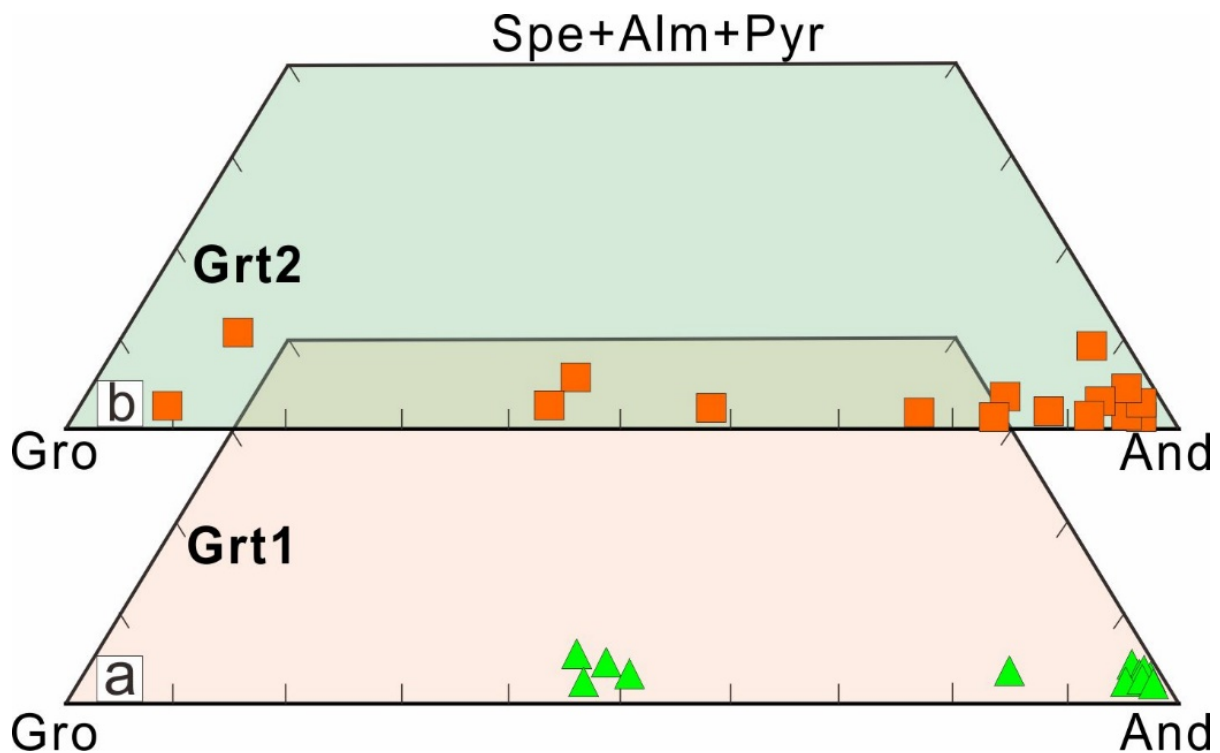
Figure 8. Triangular classification of garnets in the Niukutou deposit (the base diagram is modified from [25]) (**a**) Grt1–garnets of the first generation with relative enrichment of andradite, represented by green triangles; (**b**) Grt2–garnets of the second generation with dramatic changes in end-member compositions (andradite and grossular), represented by red squares.

Grt1 had narrow compositional ranges of SiO_2 and CaO but wide compositional ranges of FeO^T and Al_2O_3. The contents of MnO and MgO were remarkably low (less than 1%). The end-member composition of Grt1 showed wide changes consisting of $And_{45.08-99.39}Gro_{0.00-51.55}$ with minor $Pys_{0.61-3.94}$ (Figure 8a). Well-preserved chemical growth zonations and their analysis results generally showed a decrease in the FeO^T or andradite contents and an increase in the Al_2O_3 or grossular contents from the core to the rim (Figure 9a,b). From the core to the rim, there were slight increases in the MnO content, with negligible changes in TiO_2 and MgO (Figure 9a,b).

Compared to Grt1, Grt2 showed an unzoned character and dramatic changes consisting of $And_{7.60-97.67}Gro_{2.12-91.36}$ (Figure 8b), with minor $Pys_{0.24-10.28.}$ Some Grt2 showed slight changes from the core to the rim. Some Grt2 showed "M" and "W" patterns in the variations of the FeO^T (or andradite) and Al_2O_3 (or grossular) contents (Figure 9c,d), respectively, from the core to the rim. These features indicate multi-stage growth. In general, there was a negative correlation between the FeO^T and Al_2O_3 contents in the Niukutou garnets. The MnO content had the same change trend as the Al_2O_3 content, whereas the changes in TiO_2 and MgO were negligible (Figure 9c,d).
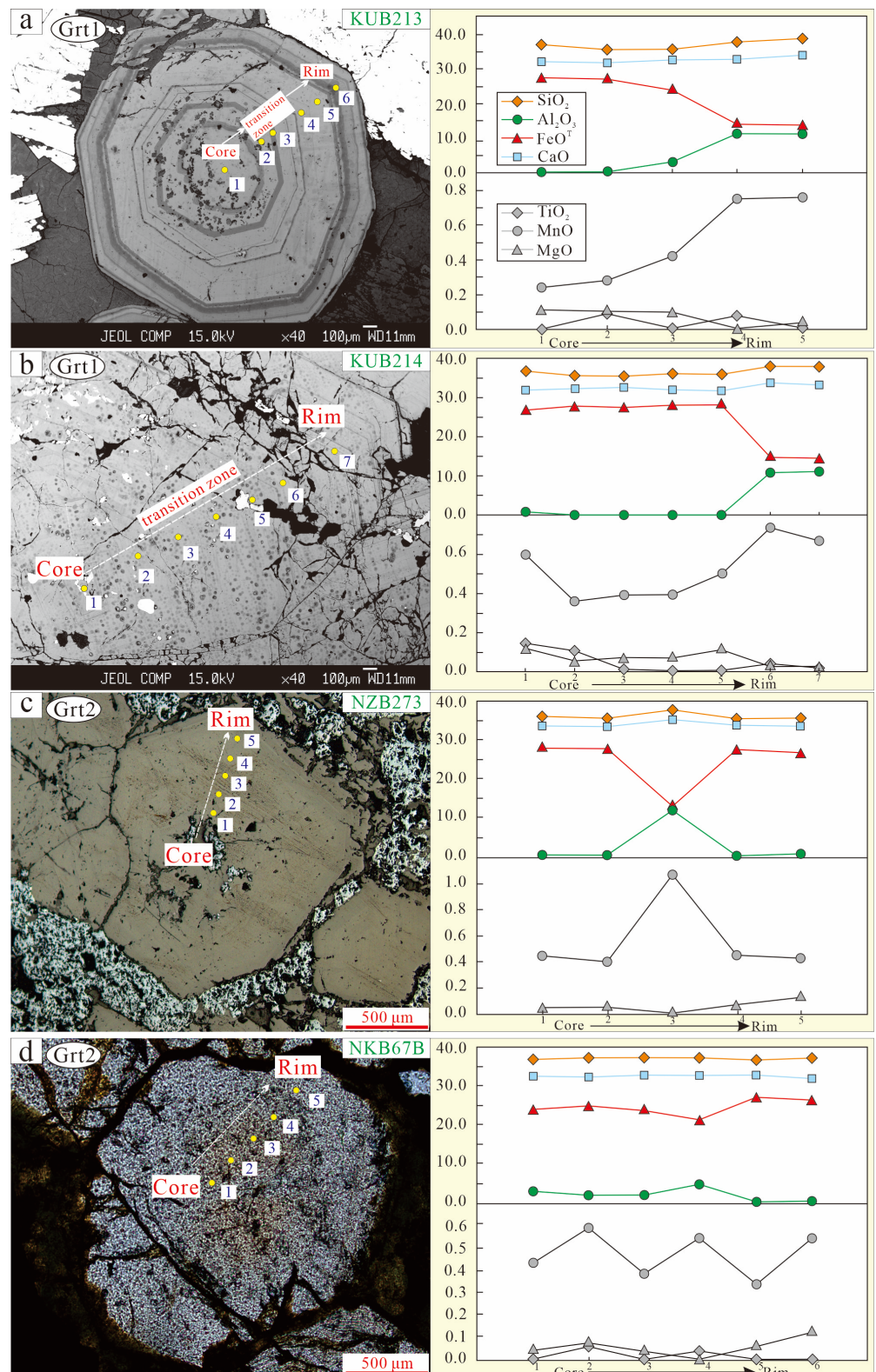
Figure 9. Back-scattered electron and cross-polarized light images for different generations of garnets and their compositional profiles in the Niukutou deposit. (**a**) Back-scattered electron image and electron probe point position of Grt1; (**b**) Back-scattered electron image and electron probe point position of Grt1; (**c**) Reflected light image and electron probe point position of Grt2; (**d**) cross-polarized light image and electron probe point position of Grt2. Notes: Numbers of 1, 2, 3, 4, 5 is referred to the position of electron probe analysis.

5.1.2. Pyroxene

As shown by the EMPA results (Table S2), Px1 had high contents of SiO_2 and CaO, with SiO_2 = 48.11%–52.75% and CaO = 18.70%–22.44%. It had a variable FeO^T (10.09%–25.50%) content and low MgO (0.62%–11.53%) and MnO (0.99%–4.44%) contents. In terms of the components calculated by the johannsenite–hedenbergite–diopside end members [26], Px1 ($Di_{5-65}Hd_{32-80}Jo_{3-15}$) was largely composed of hedenbergite, with small amounts of diopside and johannsenite (Figure 10).
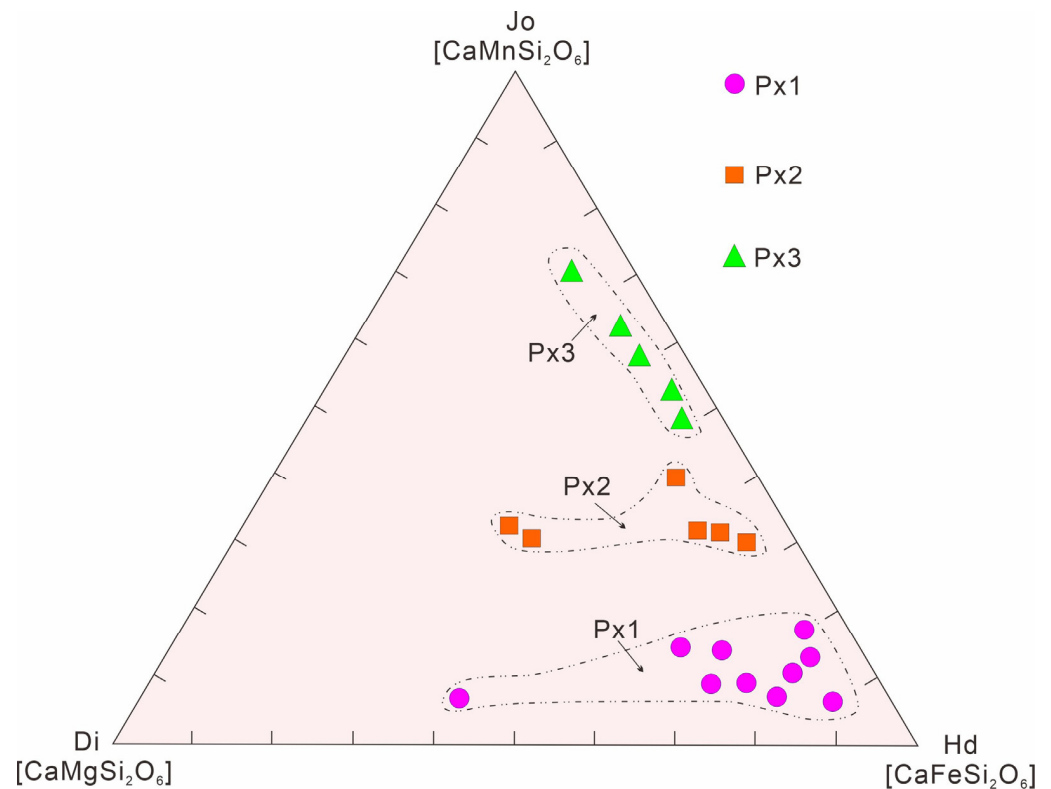
Figure 10. Ternary plots showing the end-member compositions of pyroxenes in the Niukutou deposit.

Compared to Px1, Px2 had relatively invariable contents of SiO_2 (48.64%–50.09%) and CaO (18.70%–23.93%); it also had a variable FeO^T (14.29–21.90) content and low MgO (0.06%–9.24%) and Al_2O_3 (0.01%–0.61%) contents. Regarding the MnO content, Px2 could be distinguished from Px1 by its high MnO content (6.45%–14.33%). Px2 was largely composed of hedenbergite ($Di_{6-14}Hd_{67-89}Jo_{4-19}$, Figure 10), with smaller amounts of diopside and johannsenite.

Px3 contained SiO_2 (48.32%–49.24%), FeO^T (9.28%–15.75%), CaO (18.29%–21.32%), and MnO (12.60%–19.44%). In terms of the components calculated by the johannsenite–hedenbergite–diopside end members [26], Px3 ($Di_{2-4}Hd_{31-53}Jo_{43-65}$) was composed of johannsenite and hedenbergite, with a small amount of diopside (Figure 10).

5.1.3. Ilvaite

The EMPA results (Table S3) indicated that ilvaite contained constant SiO_2 (29.45%–30.84%), CaO (12.73%–14.10%), and variable FeO^T (38.58%–48.45%) and Mn (1.78%–13.27%), with small amounts of MgO (0.02%–0.25%) and Al_2O_3 (0.06%–1.28%). From Ilv1 to Ilv3, the MnO content increased and the FeO content decreased (Figure 11). In the Mn–ilvaite and ilvaite end members (Figure 11a), Ilv3 showed the highest composition of Mn–ilvaite (21%–38%), followed by Ilv2 and Ilv1 (Figure 11b,c), with the Mn–ilvaite at 14.99%–17.14% and 5.63%–11.57% (Table S3). All these results indicate the existence of a continuous solid-solution series between ilvaite and manganilvaite (Figure 11).
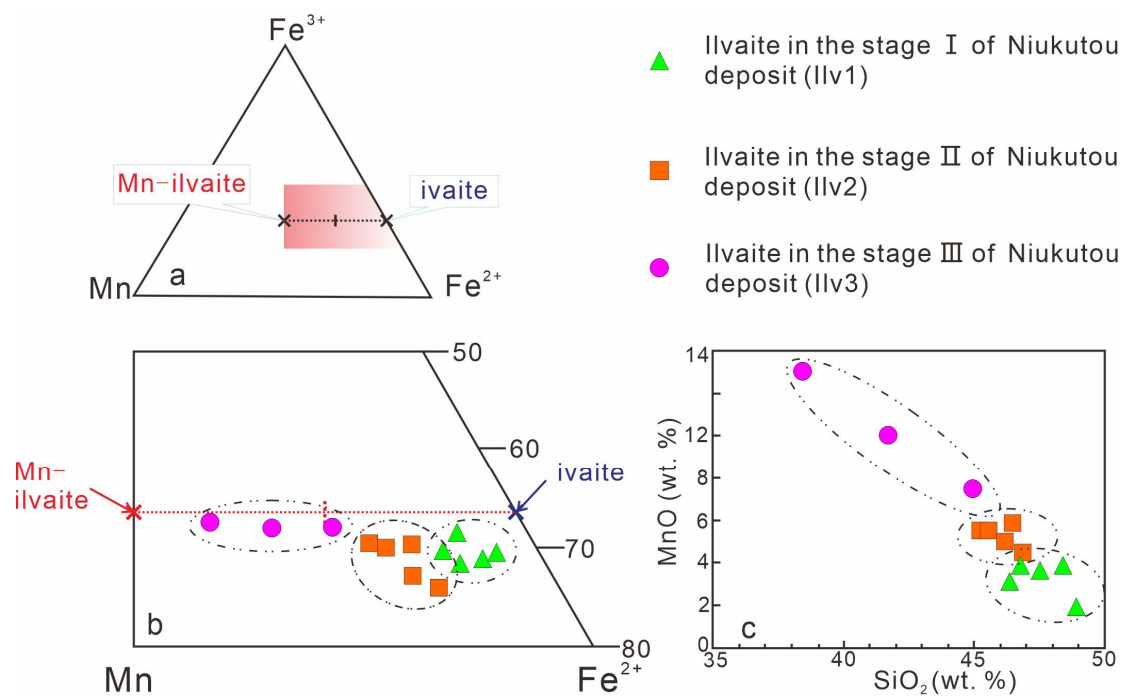
Figure 11. Diagram of Mn–Fe^{2+}–Fe^{3+} components of three generations of ilvaite (**a**,**b**), and SiO_2–MnO contents (**c**) of Niukutou for three generations of ilvaites (modified from [27]).

5.1.4. Epidote

The EMPA results (Table S4) showed that the main components of epidote were SiO_2 (37.8%–39.06%), Al_2O_3 (22.64%–26.22%), Cao (22.84%–23.76%), and FeO^T (7.83%–11.96%), percentages that fall within the ranges of the epidote group.

5.1.5. Chlorite

The EMPA results (Table S4) showed that the composition varied little; the content of SiO_2 ranged from 25.53 to 26.32%; the content of MgO ranged from 8.33 to 8.97%; the content of FeO^T ranged between 32.00 and 32.50%, and Al_2O_3 varied from 18.65 to 18.78% (Supplementary Table S4). On the chlorite classification diagram (not shown), chlorite from the Niukutou deposit is within the range of iron-magnesium chlorite.

5.2. Trace Elements

The trace element analysis by LA-ICP-MS in the Niukutou deposit was based on the different generations of garnets, pyroxenes, and ilvaites. Each generation was analyzed, and their chemical compositions are presented in Table S5.

Grt1 had medium total rare earth element (ΣREE = 3.22–155.53 ppm) contents and high fractionation between the light and heavy rare earth elements (LREE/HREE = 0.69–152.48), with variable positive Eu anomalies (δEu = 1.38–19.58) and nearly positive Ce anomalies (0.95–1.56). The chondrite-normalized REE patterns of Grt1 showed a relatively right-leaning LREE segment and a flat HREE segment (Figure 12a).

Grt2 had low total rare earth element (ΣREE = 10.55–32.63 ppm) contents and high fractionation between the light and heavy rare earth elements (LREE/HREE = 0.44–5.00), with nearly positive Eu anomalies (δEu = 0.83–1.67) and variable Ce anomalies (0.54–1.22). Unlike Grt1, the Chondrite-normalized REE patterns of Grt2 showed a relatively right-leaning LREE segment and a flat HREE segment (Figure 12a).
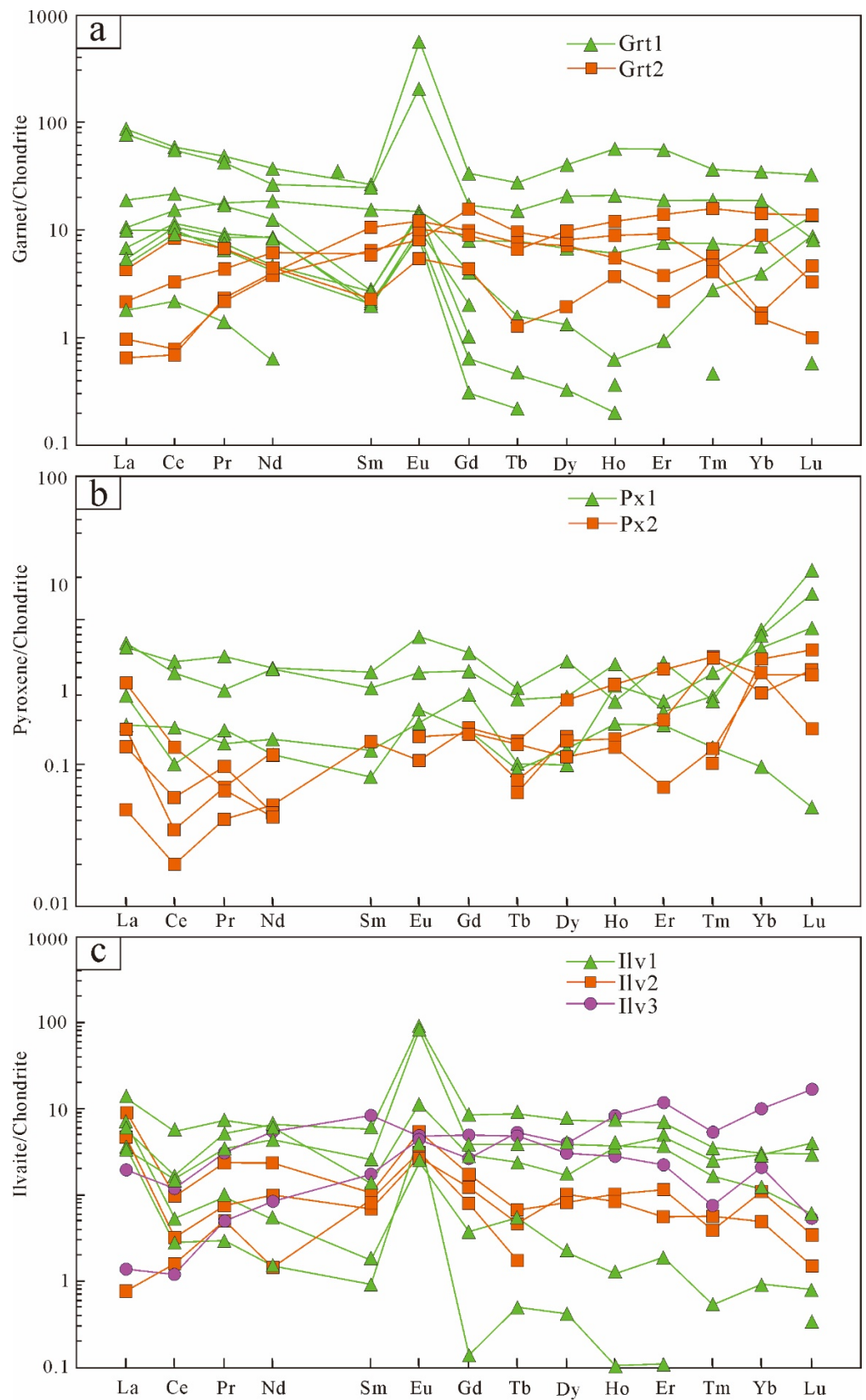
Figure 12. Chondrite-normalized rare earth element (REE) distribution patterns for different generations of garnet (**a**), pyroxene (**b**), and ilvaite (**c**) from the Niukutou deposit. The chondrite-normalized values were calculated in [28].

Px1 had low total rare earth element (ΣREE = 3.65–5.45 ppm) contents and high fractionation between the light and heavy rare earth elements (LREE/HREE = 0.26–1.76), with variable positive Eu anomalies (δEu = 0.44–1.74) and nearly positive Ce anomalies (0.44–1.99). The chondrite-normalized REE patterns of Px1 showed a relatively flat LREE segment and a left-leaning HREE segment (Figure 12b). On the whole, the REE patterns of Px1 were relatively flat.

Px2 had low total rare earth element (ΣREE = 0.65–1.65 ppm) contents and high fractionation between the light and heavy rare earth elements (LREE/HREE = 0.38–1.18), with variable positive Eu anomalies (δEu = 1.10–1.48) and variable Ce anomalies (0.22–1.12). The chondrite-normalized REE patterns of Px2 showed a relatively right-leaning LREE segment and a relatively right-leaning HREE segment (Figure 12b).

Ilv1 had total rare earth element (ΣREE = 5.22–44.29 ppm) contents and low fractionation between the light and heavy rare earth elements (LREE/HREE =1.57–32.45), with clearly positive Eu anomalies (δEu = 5.61–53.19) and nearly positive Ce (δCe = 0.28–0.54). The Chondrite-normalized REE patterns of Ilv1 showed a relatively flat LREE segment and HREE segment (Figure 12c).

Ilv2 had total rare earth element (ΣREE = 0.71–18.34 ppm) contents and high fractionation between the light and heavy rare earth elements (LREE/HREE = 2.31–3.47), with variable positive Eu anomalies (δEu = 2.41–3.70) and nearly positive Ce anomalies (δCe = 0.25–0.76). The Chondrite-normalized REE patterns of Ilv2 showed a steep right-leaning LREE segment and a flat HREE segment (Figure 12c).

Ilv3 had total rare earth element (ΣREE = 7.44–8.43 ppm) contents and high fractionation between the light and heavy rare earth elements (LREE/HREE = 0.16–1.97), with variable positive Eu anomalies (δEu = 0.73–1.95) and nearly positive Ce anomalies (δCe = 0.46–0.50). The Chondrite-normalized REE patterns of Ilv3 showed a relatively right-leaning LREE segment and a flat HREE segment (Figure 12c).

6. Discussion

6.1. Physicochemical Conditions

6.1.1. Fluid Properties

During the ore-forming processes in the skarn deposits, the mineral composition is sensitive to the changes in the hydrothermal fluid composition. Thus, the skarn minerals provide a continuous chemical record of the hydrothermal processes [29].

Grt1 in the prograde phase showed variations in composition and had andradite-rich cores with oscillatory zoning, reflecting a high prograde temperature [30] depletion in the HREE and variable Eu anomalies. The characteristics of the REEs from Grt1 and Px1 were similar to those resulting from REE partitioning in high-temperature fluids and silicate melts (relative enrichment of LREEs, depletion of HREEs, and variable Eu anomalies), implying that the ore-forming fluid in Stage 1 was derived from a magmatic–hydrothermal source [31,32]. This interpretation was confirmed by the abrupt compositional variations between the core and the rim that were interpreted as changes in the composition-dependent fluid influx [29,33].

In the magmatic–hydrothermal fluids, the Y and REEs and the Y and Ho had similar geochemical properties and showed linear correlations. The Niukutou Grt1 and Px1 samples from Stage 1 exhibited clear linear correlations between the REEs and Y and Ho (Figure 13a,b), likely indicating that there were insignificant changes in the fluid evolution, which could be interpreted as the result of the magmatic–hydrothermal source.

The Niukutou Grt2 and Px2 samples from Stage 2, however, showed insignificant correlations between the REEs and Y (Figure 13a,b), which could reflect either local protolith chemical heterogeneities or changes in the fluid composition during Stage 2 [18,34]. Moreover, the fractionation of the Y and Ho twin pairs from the chondritic ratio (Figure 13b) was an indication that Grt2/Px2 assemblage growth occurred in a complex hydrothermal fluid system [35,36]. Moreover, the unstable composition of the Stage 2 minerals may have

been due to their position in the upper part of the contact metamorphic belt, as they would have been affected by multiple-contact metasomatism.
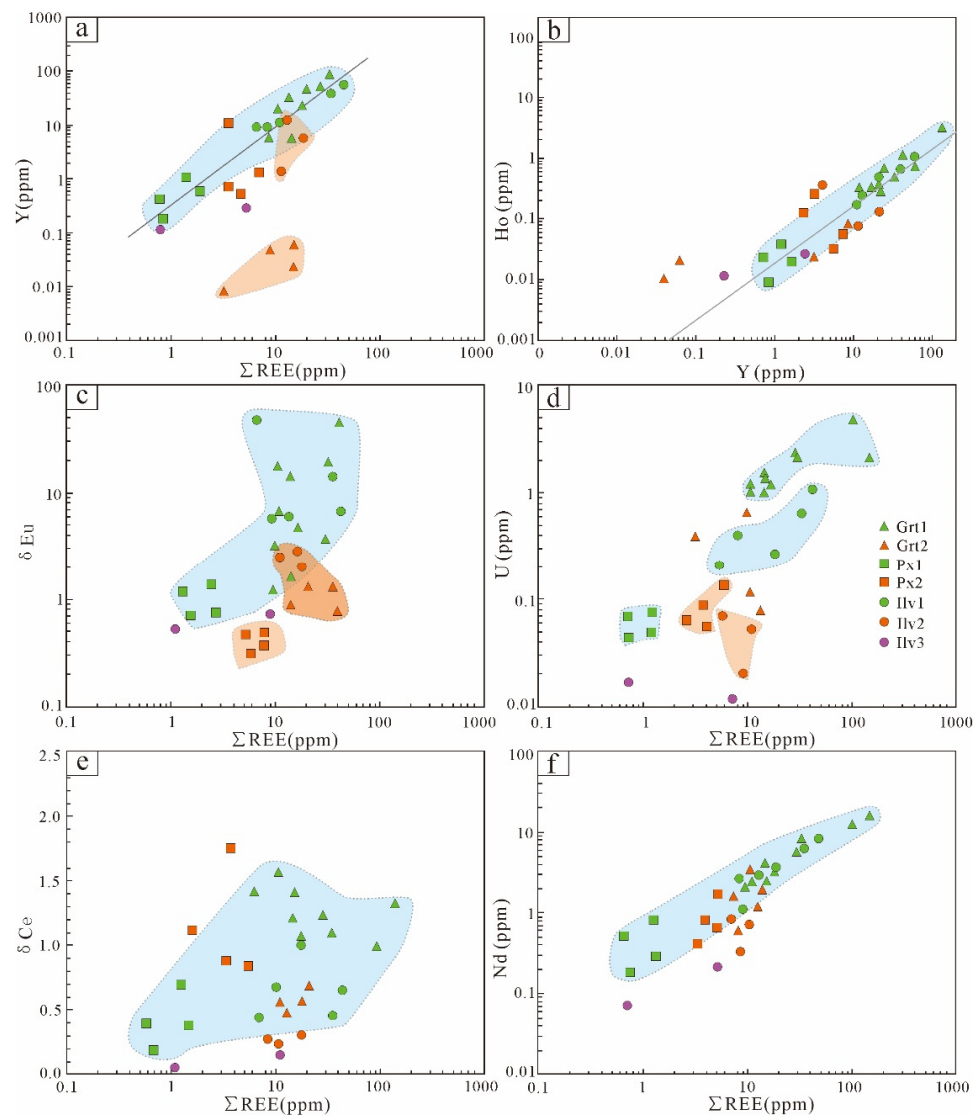
Figure 13. Binary plots of (**a**) Y versus total rare earth element (∑REE), (**b**) Ho versus Y, (**c**) δEu versus ∑REE, (**d**) U versus ∑REE, (**e**) δCe versus ∑REE, (**f**) δCe versus ∑REE.

The representative quartz + sulfides and quartz + calcite veins that cut the johannsenite (Px3) mineral assemblages (Figures 6l and 7h) signify that the ore-forming fluid in Stage 3 was generated under low-temperature conditions after magnetite and pyrrhotite precipitation. Although Px3 was present in Stage 3, it had low ∑REE, Y, and Y/Ho contents and a high HFSE (high-field strength element) content, and this disparity resulted from the differences in the fluid composition and fluid flow rate [20].

In summary, the Grt1 and Px1 skarn mineral assemblages in Stage 1 resulted from a magmatic–hydrothermal source; the Grt2 and Px2 skarn minerals in Stage 2 may have been caused by a fluid system that was altered by either local protolith chemical heterogeneities or changes in the fluid composition, and the Px3 in Stage 3 may have been generated in a more complex environment with a more variable fluid composition and fluid flow rate.

6.1.2. Oxygen Fugacity

Prograde Metamorphic Phase

Generally, in a hydrothermal system, the Eu^{3+}/Eu^{2+} distribution coefficients are essentially independent of the major cation chemistry of the solution, whereas for altervalent substitutions, they are not. Thus, the δEu anomalies of the minerals can be used to evaluate the redox conditions of the fluid [18,32,37–43]. In addition, based on the similar ion radii and charge balances, reducing the fO_2 can reduce the solubility of U, which facilitates the entrance of U into the mineral crystal. Thus, the different U concentrations of the minerals could indicate the relative fO_2 of the fluid.

From Stage 1 to Stage 3, the δEu and U contents of the garnet and pyroxene gradually decreased (Figure 13c,d), indicating that the oxidizing ability of the environment decreased accordingly. Specifically, an oxidizing environment is favorable for the generation of magnetite. This interpretation is supported by the replacement of Grt1 with magnetite. Subsequently, with the decreasing fO_2, the environment of the ore-forming fluid became more reduced and thus favorable for the dissolution and precipitation of Pb-Zn sulfide minerals.

In addition, according to previous studies [44,45], we constructed a temperature-log fO_2 phase diagram (Figure 14) of the Ca-Fe-Si-O-H-C system. The hydrothermal fluid system in Stage 1 (Grt1+Px1) had temperatures ranging from 400 to 470 °C, and logfO_2 values ranging from −23.8 to −19. The simulated temperatures in Stages 2 and 3 were 410–440 and 340–400 °C, respectively, and the corresponding logfO_2 values ranged from −23–19.5 to −27–23.5, respectively. Generally, these features reflect decreasing fO_2 and temperatures.
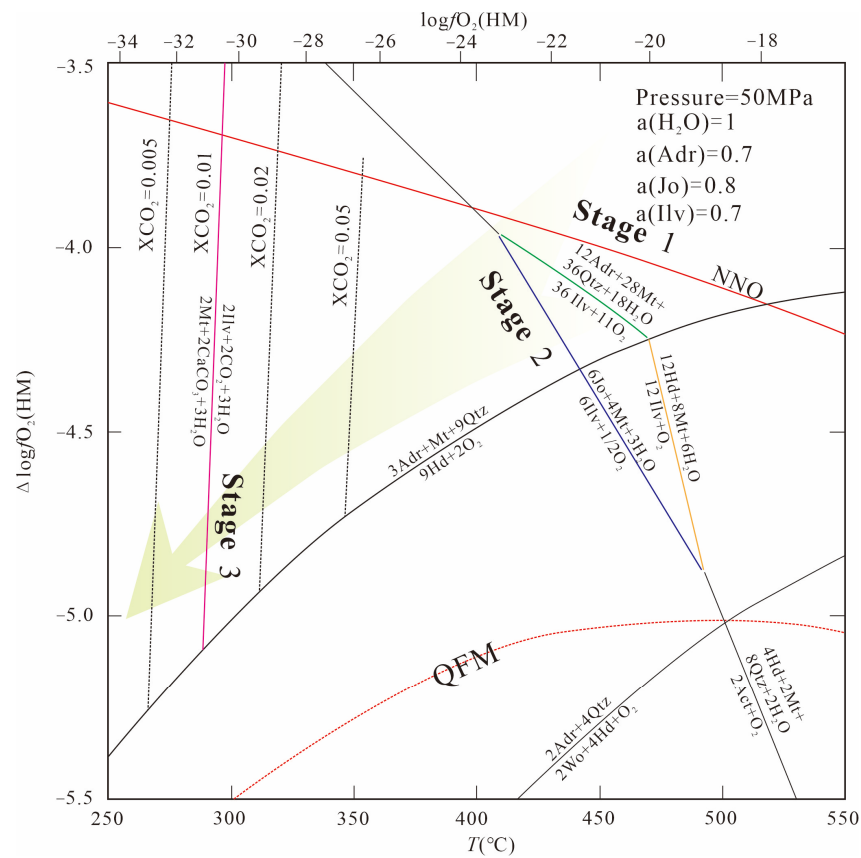
Figure 14. Temperature-log fO_2 diagram for the Ca–Fe–Si–O–H–C system (modified from [44]). Reactions involving ilvaite are in bold; dotted red lines correspond to the indicated mineral buffer. The arrow indicates the postulated trajectory of fO_2 during skarn development.

Retrograde Metamorphic Phase

The three types of ilvaites in the retrograde metamorphic stage from the inside to the outside were successively distributed in the andradite–hedenbergite skarn belt (inner belt), the grossular–mangan–hedenbergite belt (middle belt), and the johannsenite skarn belt (outer belt). They correspond to three generations of a retrograde metamorphic stage.

From Ilv1 to Ilv3, the δEu and U contents were also decreasing (Figures 12c and 13d,e), indicating that the oxygen fugacity of mineralization was decreasing. With the decrease in oxygen fugacity, the ore-forming fluid environment rapidly decreased, ultimately facilitating the dissolution and precipitation of Pb and Zn elements.

6.1.2.3. pH
Prograde Metamorphic Phase

In addition to the fluid properties of a hydrothermal system, the temperature, cation type, and fluid density also play important roles in the pH of the fluid. Therefore, it is inappropriate to separately describe the pH based on the fluid composition [46]. Fortunately, the REEs and some immobile trace elements in hydrothermal fluids are scarcely affected in magmatic–hydrothermal fluids and pH is largely correlated with their total contents in the fluid [35,47]. It was demonstrated in [38] that LREE-depleted and HREE-enriched patterns with negative or no Eu anomalies form under nearly neutral pH, whereas LREE-enriched and HREE-depleted patterns develop under mildly acidic pH, and the Eu anomalies are positive or significantly controlled by the complexing agents (mainly F, Cl, and B). The Niukutou Grt1 crystals are characterized by an enrichment of LREEs and a depletion of HREEs and have mostly positive Eu anomalies, indicating a mildly acidic pH environment. In comparison, the Grt2 crystals show an enrichment of HREEs and a depletion of LREEs and negative or no Eu anomalies, suggesting nearly neutral pH conditions. The Px3 crystals have relatively more variable LREE/HREE ratios and Eu anomalies, suggesting a more neutral pH in Stage 3.

An investigation [47] of thermal fluids found that pH strongly controls the changes in the REE and Ce anomalies and shows negative correlations with the REEs and Ce. Moreover, theoretical and thermodynamic experiments have suggested that pH significantly affects the fractionation of REEs and Nd and that pH is negatively correlated with the REEs and Nd in hydrothermal fluids [38,48]. An early increasing trend followed by a decreasing trend for the REEs, Ce, and Nd contents from Stage 1 to Stage 3 (Figure 13e,f), indicates an increase in pH during the evolution of the Niukutou hydrothermal fluid.

These changes in pH suggest that the low acidic pH conditions in the early stages (Stage 1) were favorable for the enrichment and mineralization of Fe contents.

Retrograde Metamorphic Phase

From Ilv1 to Ilv3, the trace elements changed from being rich in LREEs, depleted in HREEs, and with a positive Eu anomaly to a variable LREE/HREE ratio and δ Eu anomaly. With the REEs, the Nd contents and δ Ce gradually increased, suggesting that the pH value of the fluid environment in the retrograde metamorphic phase gradually decreased.

6.2. Ore-Forming Fluid Evolution

The mineral assemblages of the Niukutou deposit and their geochemical characteristics may reflect the evolution of the hydrothermal fluid. Under a low degree of water–rock reactions in closed conditions, hydrothermal evolution is dominated by diffusion metasomatism, whereas under the conditions of open systems, the evolution is dominated by infiltration metasomatism [32]. The REEs and trace elements of skarn minerals can indicate the nature and evolution of ore-forming fluids [37,49].

The Niukutou Grt1/Px1 in Stage 1 exhibited low LILE and high HFSE and Y-Ho contents. The results suggested that Grt1 was formed under a relatively stable and closed environment with a low degree of water–rock reaction. In addition, the Grt1/Px1/Ilv1 system had a good crystal shape, indicating a slow rate of hydrothermal migration and

crystal growth. In combination with the linear correlation of the Y/REE and Y/Ho ratios, the chemical features suggested that the evolution of the ore-forming fluids produced magmatic–hydrothermal fluids. Based on the above information, we suggest that the generation of the Grt1/Px1 system was mainly via diffusive metasomatism.

Compared to Grt1/Px1, the Y, Ho, and HFSE contents of Grt2/Px2 showed a wide range, suggesting that these minerals were generated under the circumstances of exhumation from very high-grade conditions. Such dynamic and repetitive enrichment and depletion of composition require the fluid flow to have been episodic, possibly caused by periods of metasomatism between the hydrothermal fluid and the wall rocks [29].

Grt2/Px2 had poor crystal form, showed a depletion of LREEs and an enrichment of HREEs, and had variable Eu anomalies, all of which imply the addition of external fluids. The Y/REE and Y/Ho twin pairs from the chondritic ratios are indications that Grt2/Px2 growth occurred in a complex hydrothermal fluid system with a strong degree of water–rock action.

Additionally, evidence from the incomplete crystallization of Grt2/Px2 in Stage 2 showed that the upper skarn zoning developed with pervasive ore-guiding structures. Our results suggested an infiltrative metasomatism with the introduction of a batch of externally derived fluid.

The ilvaite coexisting with the garnet and pyroxene had similar REE patterns. For example, Ilv1 was consistent with the Grt1/Px1 assemblages due to the positive Ce and negative Eu anomalies. This evidence implies that retrograde ilvaite inherited prograde skarns during the hydrothermal process. Based on their coexisting mineral-associated relationships, we conclude that the replacement of prograde garnet/pyroxene probably accounts for the generation of ilvaite in the late phase.

6.3. Implications for Mineralization

As previously noted, the composition of Px1 and Px2 in the Niukutou deposit was johannsenite (Jo, 22%–65%), hedenbergite (31%–74%) and small amounts of diopside (3%–42%), and MnO (6.92%–19.44%), indicating Mn-rich mineral characteristics. In addition, the MnO contents of the Niukutou ilvaites were 1.78%–13.27%, which were higher than those in common ilvaites (Figure 9). Thus, we can infer that the Niukutou skarn is a manganese-type skarn. Many studies have shown that there are two skarn formations in the Qimantagh area, a calcium skarn and a manganese skarn; a calcium skarn generally forms iron polymetallic deposits and copper polymetallic deposits, whereas a manganese skarn forms Pb-Zn (Ag) deposits [45,50–57]. Skarns worldwide have similar characteristics.

In the ternary plot diagrams, it can be seen that the garnet and pyroxene composition plots in specific fields had almost the same range as the typical Pb-Zn skarn deposits in the Qimantagh area such as the Weibao and Sijiaoyang Pb-Zn skarn deposits. However, the Niukutou skarn deposit can be distinguished from these Fe and Cu skarns (Yemaquan and Kaerqueka) by its distinctive mineralogical characteristics and relatively wide range of garnet composition and Mn-rich mineralogical characteristics (Figure 15a,b). All these characteristics indicate that the Niukutou skarn deposit has the potential for Pb-Zn mineralization.

The evidence from the mineral geochemical characteristics showed that Grt1/Px1 in the Stage 1 zonation deposit occurred in the deepest layers with the highest $f\text{O}_2$ and temperatures and a low acidic pH. The skarn minerals were characterized by andradite and hedenbergite, and the mineralization was characterized by magnetite, pyrrhotite, and chalcopyrite.

Grt2/Px2 in the Stage 2 deposit in the middle part indicated moderate $f\text{O}_2$ and temperatures, an acidic to neutral composition, and a relatively higher pH. The skarn minerals were characterized by grossular features and Mn–Hd, whereas the mineralization was characterized by pyrrhotite, sphalerite, and galena.
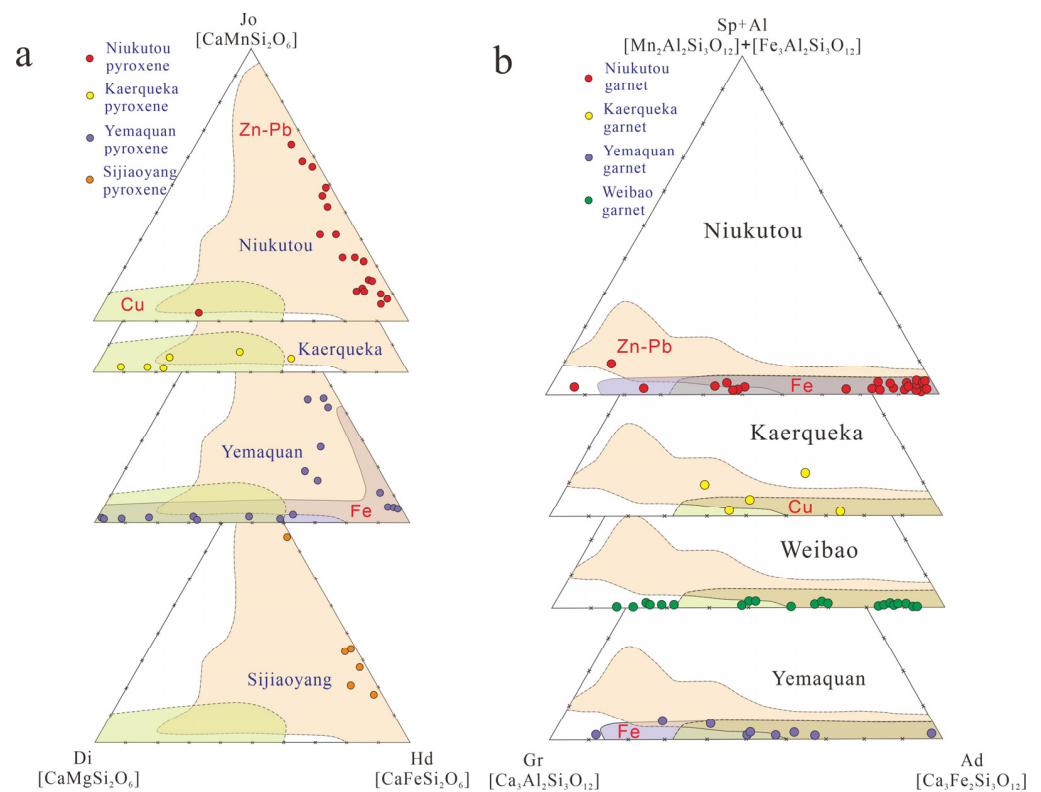
Figure 15. Ternary plots showing the end-member compositions of pyroxenes (**a**) and garnets (**b**) from the Niukutou deposit, Qimantagh area (modified after [7]). Data sources: Niukutou, this study; Kaerqueka, Hutouya, and Yemaquan from Feng et al. [21]; Sijiaoyang, [1,50]). Weibao, Kaerqueka, and Hutouya are typical Cu-Pb-Zn skarn deposits in the QMB, whereas Yemaquan and Sijiaoyang are Fe-Cu-Zn and Pb-Zn skarn deposits, respectively. The areas for global Cu, Fe, and Pb-Zn skarn deposits are from Meinert et al. [26]. End members: Jo—johannsenite, Di—diopside, Hd—hedenbergite, Ad—andradite, Gr—grossular, Sp—spessartine, Al—almandine.

The Ilv3 or johannsenite (Px3) deposits in the uppermost part showed low fO_2 and temperatures and had neutral pH compositions. The skarn minerals were characterized by manganilvaite and johannsenite, and the mineralization was characterized by sphalerite and galena.

According to the geochemical characteristics, Grt1/Px1 exhibited low LILE and high HFSE and Y-Ho contents, a strong linear correlation between the Y/REE and Y/Ho ratios, and good crystal shapes, indicating that the metasomatization of the Grt1/Px1 skarn zonation was primarily diffusive metasomatism near the ore-related pluton and that hydrothermal evolution occurred under closed conditions. The Grt2/Px2 deposits showed depletion of LREEs, enrichment of HREEs, and variable Eu anomalies, and the Y/REE and Y/Ho twin pairs deviated from the chondritic linear line and showed a wide range of compositions and incomplete crystallization of the minerals in Stage 2. These observations suggested that Stage 2 was dominated by infiltrative metasomatism. For an open system, this evolutionary interpretation is supported by the pervasive vertical fractures in the middle and upper parts of the skarn zoning.

The three mineral assemblages correspond to three skarn zonations, and these zonation sequences are characterized as follows, moving outward from the intruding granodiorite intrusion: Grt1+Px1+Ilv1 skarn–Grt2+Px2+Ilv2 skarn–Px3+Ilv3 skarn–marble. Fe-S-Cu ore bodies occurred in the Grt1+Px1 skarn, whereas Pb-Zn (or S) ore bodies mainly occurred in the Grt2+Px2+Ilv2 and Px3+Ilv3 skarns.

According to the spatial relationships and geochemical characteristics of the mineral assemblages, the ore-forming fluid evolution of the Niukutou deposit can be described as

follows: from Stage 1 to Stage 3, the hydrothermal fluid migration moved from the deep skarn-related plutons to the shallow skarn and marble, and the environment featured high fO_2 and temperatures to low fO_2 and temperatures and an increasing pH and Mn content (Figure 16). The three generations of ilvaites (Ilv1 to Ilv3) in the retrograde stage had the same characteristics of zonation and fluid evolution.
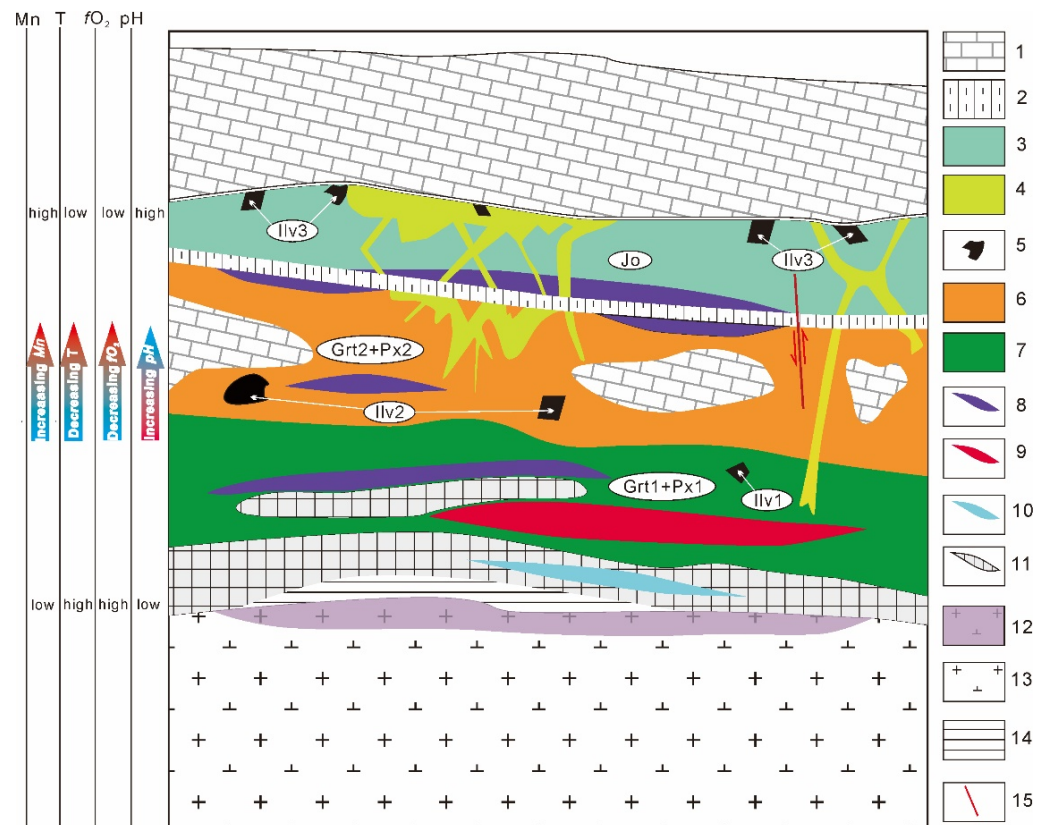
Figure 16. Profile showing the skarn zonation and evolution process of the ore-forming fluid in the Niukutou Pb-Zn skarn deposit: 1—Marble, 2—Siltstone, 3—Ilv3 + Px3 (johannsenite) skarn zoning, 4—epidote + chlorite skarn, 5—Ilvaite, 6—Grt2+Px2 skarn zoning, 7—Grt1+Px1 skarn zoning, 8—Pb-Zn ore body, 9—Fe ore body, 10—Cu ore body, 11—Pyrrhotite (S) ore body, 12—altered granodiorite pluton, 13—Granodiorite pluton, 14—Hornstone belt, and 15—Fault.

During the migration of the ore-forming fluid, magnetite, chalcopyrite, arsenopyrite, and pyrrhotite, all of which are high-temperature ore minerals, precipitated in Stage 1. The environment was favorable for the enrichment and mineralization of the Fe content [58,59]. Thus, permeability may eventually have been reduced, thereby obstructing the fluid channels [60–62]. Then, a strong pressure increase could have caused hydraulic fracturing when the hydrostatic pressure exceeded the lithostatic pressure. However, the permeability increased as fractures opened and the pressure decreased, and this, in turn, promoted mineral formation and likely created an open system for metasomatism in Stages 2 and 3.

In Stage 2, the environment changed from oxidizing conditions with a mildly acidic pH to relatively reducing conditions with a relatively neutral pH; subsequently, the Fe^{2+} and Mn^{2+} would precipitate to generate the mangan–hedenbergite. Additionally, due to the increasing pH, Al^{3+} precipitated to generate the grossular minerals. Furthermore, the environment was favorable for the precipitation of pyrrhotite and sphalerite. With the evolution of the hydrothermal fluid, the fluid became more reducing and neutral, the temperature became lower, and further enrichment in Mn occurred, leading to the highest MnO content in Stage 3 among the skarn minerals.

Similarly, from Ilv1 to Ilv3, the ore-forming environment rapidly declined. The reducing nature of the ore-forming fluid was beneficial to the deposition of the Pb-Zn complex and the precipitation and enrichment of the Mn-rich skarns; this may explain why the Pb-Zn ore bodies were closely associated with the Mn-rich skarns.

7. Conclusions

Based on the field geology, petrographic observations, and mineral geochemistry studies, the following conclusions were drawn:

(1) Three mineral assemblages in a prograde metamorphic phase and their corresponding mineralization stages were distinguished in the Niukutou deposit. From Stages 1 to 3, the temperature and fO$_2$ decreased, whereas the pH increased. The ilvaites (Ilv1 to Ilv3) in the retrograde metamorphic phase also indicate lower temperatures, decreased fO$_2$, and lower pH.

(2) The metallogenic process in Stage 1 was primarily diffusive metasomatism under a low degree of water–rock reactions in the closed condition. The ore-forming fluid in Stages 2 and 3 may have experienced infiltrative metasomatism with the introduction of a batch of externally derived fluid.

(3) The Niukutou deposit belongs to a manganese skarn pattern, and the skarn zonation and mineral geochemical characteristics show that the hydrothermal fluid migrated from the deep plutons to the shallow marble. The environments evolved from high fO$_2$ and temperatures to low fO$_2$ and temperatures and showed increasing pH and Mn contents, ultimately resulting in the close association between the Pb-Zn ore bodies and Mn-rich skarns.

References

1. Feng, C.Y.; Wang, X.P.; Shu, X.F.; Zhang, A.K.; Xiao, Y.; Liu, J.N.; Ma, S.C.; Li, G.C.; Li, D.X. Isotopic Chronology of the Hutouya Skarn Lead-Zinc Polymetallic Ore District in Qimantage Area of Qinghai Province and Its Geological Significance. *J. Jilin Univ.* **2011**, *41*, 1806–1817. (In Chinese with English abstract)
2. Feng, C.Y.; Wang, S.; Li, G.C.; Ma, S.C.; Li, D.S. Middle to late Triassic granitoids in the Qimantage area, Qinghai Province, China: Chronology, geochemistry and metallogenic significances. *Acta Petrol. Sin.* **2012**, *28*, 665–678. (In Chinese with English abstract)
3. Mao, J.W.; Zhou, Z.H.; Feng, C.Y.; Wang, Y.T.; Zhang, C.Q.; Peng, H.J.; Yu, M. A preliminary study of the Triassic large-scale mineralization in China and its geodynamic setting. *Geol. China* **2012**, *39*, 1437–1471. (In Chinese with English abstract)

4. Wang, X.Y.; Zhu, X.Y.; Li, J.D.; Wang, Y.W.; Long, L.L.; Li, S.T.; Wu, J.R.; Cheng, X.Y.; Jiang, B.B. Genesis and geological significance of manganilvaite in the Niukutou deposit, Qinghai Province. *Acta Geol. Sin.* **2020**, *94*, 2279–2290. (In Chinese with English abstract)

5. Wang, X.Y.; Zhu, X.Y.; Li, J.D.; Wang, Y.W.; Jiang, B.B.; Wu, J.R.; Huang, X.K.; Zhao, Z.Y. Two stage magmatisms and their skarn-type mineralization in the Niukutou ore district, Qinghai Provice. *Acta Petrol. Sin.* **2021**, *37*, 1567–1586.

6. Zhong, S.H.; Feng, C.; Seltmann, R.; Li, D. Middle Devonian volcanic rocks in the Weibao Cu–Pb–Zn deposit, East Kunlun Mountains, NW China: Zircon chronology and tectonic implications. *Ore Geol. Rev.* **2017**, *84*, 309–327. [CrossRef]

7. Zhong, S.H.; Feng, C.; Seltmann, R.; Dolgopolova, A.; Andersen, J.C.Ø.; Li, D.; Yu, M. Sources of fluids and metals and evolution models of skarn deposits in the Qimantagh metallogenic belt: A case study from the Weibao deposit, East Kunlun Mountains, northern Tibetan Plateau. *Ore Geol. Rev.* **2018**, *93*, 19–37. [CrossRef]

8. Gao, Y.B.; Li, W.Y.; Qian, B.; Li, K.; Li, D.S.; He, S.Y.; Zhang, Z.W.; Zhang, J.W. Geochronology, geochemistry and Hf isotopic compositions of the granitic rocks related with iron mineralization in Yemaquan deposit, East Kunlun, NW China. *Acta. Petrol. Sin.* **2014**, *30*, 1647–1665. (In Chinese with English abstract)

9. Yu, M.; Feng, C.Y.; Bao, G.Y.; Liu, H.C.; Zhao, Y.M.; Li, D.X.; Xiao, Y.; Liu, J.N. Characteristics and zonation of skarn minerals in Galinge iron deposit, Qinghai Province. *Miner. Depos.* **2013**, *32*, 55–76. (In Chinese with English abstract)

10. Yu, M.; Feng, C.Y.; Mao, J.W.; Santosh, M.; Zhu, Y.F.; Zhao, Y.M.; Li, D.X. The Qiman Tagh Orogen as a window to the crustal evolution in northern Tibetan Plateau. *Earth Sci. Rev.* **2017**, *167*, 103–123. [CrossRef]

11. Zhao, Y.M.; Tan, H.J.; Xu, Z.N.; Yuan, C.G.; Bi, C.S.; Zheng, R.L.; Li, D.X.; Sun, J.H. The calcic-skarn iron ore deposits of Makeng type in southwestern Fujian. *Bull. Inst. Miner. Depos. Chin. Acad. Geol. Sci. (Album)* **1983**, *1*, 1–141. (In Chinese with English abstract)

12. Zhong, S.H.; Feng, C.; Seltmann, R.; Li, D.; Dai, Z. Geochemical contrasts between Late Triassic ore-bearing and barren intrusions in the Weibao Cu–Pb–Zn deposit, East Kunlun Mountains, NW China: Constraints from accessory minerals (zircon and apatite). *Miner. Depos.* **2018**, *53*, 855–870. [CrossRef]

13. Zhong, S.H.; Feng, C.; Seltmann, R.; Li, D.; Qu, H. Can magmatic zircon be distinguished from hydrothermal zircon by trace element composition? The effect of mineral inclusions on zircon trace element composition. *Lithos* **2018**, *314–315*, 646–657. [CrossRef]

14. Jian, R.T.; Zhao, X.K.; Yang, F.; Li, J.D.; Wu, J.R. New progress in prospecting for Niukutou iron polymetallic deposit, Qinghai. *Acta Mineral. Sin.* **2017**, *34*, 821–823. (In Chinese with English abstract)

15. Li, J.D.; Wang, X.Y.; Zhu, X.Y.; Wu, J.R.; Cai, Y.W.; Li, Y.; Guo, T.J.; Jiang, B.B. Finding and significance of ilvaite in the Qimantag area-with the example of Niukutou lead and zinc deposit. *Min. Explor.* **2019**, *10*, 1550–1558. (In Chinese with English abstract)

16. Li, J.D.; Wang, X.Y.; Zhu, X.Y.; Wu, J.R.; Cai, Y.W.; Li, Y.; Guo, T.J.; Jiang, B.B. The preliminary discussion of the Hercynian metallogenic period in Qimantag area–with the example of Niukutou lead and zinc deposit. *Min. Explor.* **2019**, *10*, 1775–1783. (In Chinese with English abstract)

17. Zhao, X.K.; Jian, R.T.; Yu, C.; Yang, F.; Li, J.D. Geological Characteristics and Prospecting Indicators of Niukutou Fe-Pb-Zn Polymetallic Deposit in Qinghai Province. *Mor. Min.* **2018**, *585*, 10–16. (In Chinese with English abstract)

18. Gaspar, M.; Meinert, L.D.; Moretti, R. REE in skarn systems: A LA-ICP-MS study of garnets from the Crown Jewel gold deposit. *Geochim. Cosmochim. Acta* **2008**, *72*, 185–205. [CrossRef]

19. Zhai, D.G.; Liu, J.J.; Zhang, H.Y.; Wang, J.P.; Su, L.; Yang, X.A.; Wu, S.H. Origin of oscillatory zoned garnetsfrom the Xieertala Fe–Zn skarn deposit, northern China: In situ LA-ICP-MS evidence. *Lithos* **2014**, *190*, 279–291. [CrossRef]

20. Baghban, S.; Hosseinzadeh, M.; Moayyed, M.; Mokhtari, A.A.; Gregory, D.D. Geology, mineral chemistry and formation conditions of calc-silicate minerals of Astamal Fe-LREE distal skarn deposit, Eastern Azarbaijan province, NW Iran. *Ore Geol. Rev.* **2015**, *68*, 79–96. [CrossRef]

21. Feng, C.Y.; Yu, M.; Li, D.X.; Li, G.C.; Zhou, A.S.; Li, X. Fluid inclusion geochemistry of Bashierxi tungsten-tin deposit in Qimantag area, Xinjiang. *Miner. Depos.* **2013**, *32*, 20–36. (In Chinese with English abstract)

22. Gao, Y.B. The Intermediate-Acid Intrusive Magmatism and Mineralization in Qimantag, East Kunlun Mountains. Ph.D. Thesis, Chang'an University, Xi'an, China, 2013.

23. Lu, Y.F. Geokit: Geochemical software package built by VBA. *Geochemistry* **2004**, *33*, 459–464. (In Chinese with English abstract)

24. Brandelik, A. CALCMIN-an EXCELTM Visual Basic application for calculating mineral structural formulae from electron microprobe analyses. *Comput. Geosci.* **2009**, *35*, 1540–1551. [CrossRef]

25. Meinert, L.D. Skarns and skarn deposits. *Geosci. Can.* **1992**, *19*, 145–162.

26. Meinert, L.D.; Dipple, G.M.; Nicolescu, S. World skarn deposits. *Econ. Geol. 100th Anniv. Vol.* **2005**, 299–336. [CrossRef]

27. Bonev, I.K.; Vassileva, R.D.; Zotov, N.; Kouzmanov, K. Manganilvaite, $CaFe^{2+}Fe^{3+}(Mn, Fe^{2+})(Si_2O_7)O(OH)$, a new mineral of the ilvaite group from Pb-Zn skarn deposits in the Rhodope Moutntains, Bulgaria. *Can. Mineral.* **2005**, *43*, 1027–1042. [CrossRef]

28. Sun, S.S.; McDonough, W.F. Chemical and isotopic systematic of oceanic basalts: Implications for mantle composition and processes. *Geol. Soc. Lond. Spec. Publ.* **1989**, *42*, 313–345. [CrossRef]

29. Jamtveit, B.; Wogelius, R.A.; Fraser, D.G. Zonation patterns of skarn garnets: Records of hydrothermal system evolution. *Geology* **1993**, *21*, 113–116. [CrossRef]

30. Dietvorst, E.J.L. Retrograde garnet zoning at low pressure in metapeletic rocks from kemio, SW Finland. *Contrib. Mineral. Petrol.* **1982**, *79*, 37–45. [CrossRef]

31. Flynn, R.T.; Burnham, C.W. An experimental determination of rare earth partition coe_cients between a chloride containing vapor phase and silicate melts. *Geochim. Cosmochim. Acta.* **1978**, *42*, 685–701. [CrossRef]

32. Park, C.P.; Song, Y.G.; Kang, I.M.; Shim, J.; Chung, D.H.; Park, C.S. Metasomatic changes during periodic fluid flux recorded in grandite garnet from the Weondong W-skarn deposit, South Korea. *Chem. Geol.* **2017**, *451*, 135–153. [CrossRef]

33. Jamtveit, B.; Hervig, R.L. Constraints on transport and kinetics in hydrothermal systems from zoned garnet crystals. *Science* **1994**, *263*, 505–508. [CrossRef] [PubMed]

34. Wood, S.A. The geochemistry of rare earth elements and yttrium in geothermal waters. *Spec. Publ. Soc. Econ. Geol.* **2003**, *10*, 133–158.

35. Bau, M. Controls on the fractionation of isovalent trace elements in magmatic and aqueous systems: Evidence from Y/Ho, Zr/Hf, and lanthanide tetrad effect. *Contrib. Mineral. Petrol.* **1996**, *123*, 323–333. [CrossRef]

36. Anders, M.; Grevesse, N. 1989. Abundances of the elements: Meteoritic and solar. *Geochim. Cosmochim. Acta* **1989**, *53*, 197–214. [CrossRef]

37. Xiao, X.; Zhou, T.F.; White, N.C.; Zhang, L.J.; Fan, Y.; Wang, F.Y.; Chen, X.F. The formation and trace elements of garnet in the skarn zone from the Xinqiao Cu-S-Fe-Au deposit, Tongling ore district, Anhui province, Eastern China. *Lithos* **2018**, *302*, 467–479. [CrossRef]

38. Bau, M. Rare-earth element mobility during hydrothermal and metamorphic fluid–rock interaction and the significance of the oxidation state of europium. *Chem. Geol.* **1991**, *93*, 219–230. [CrossRef]

39. Sverjensky, D.M. Europium redox equilibria in aqueous solution. *Earth Planet. Sci. Lett.* **1984**, *67*, 70–78. [CrossRef]

40. Van Westernen, W.; Allan, N.L.; Blundy, J.D.; Purton, J.A.; Wood, B.J. Atomistic simulation of trace element incorporation into garnets–comparison with experimental garnet–melt partition data. *Geochim. Cosmochim. Acta* **2000**, *64*, 1629–1639. [CrossRef]

41. Smith, M.P.; Henderson, P.; Jeffries, T.E.R.; Long, J.; Williams, C.T. The rare earth elements and uranium in garnets from the Beinn an Dubhaich Aureole, Skye, Scotland, UK: Constraints on processes in a dynamic hydrothermal system. *J. Petrol.* **2004**, *45*, 457–484. [CrossRef]

42. Zhong, S.H.; Seltmann, R.; Shen, P. Two different types of granitoids in the Suyunhe large porphyry Mo deposit, NW China and their genetic relationships with molybdenum mineralization. *Ore Geol. Rev.* **2017**, *88*, 116–139. [CrossRef]

43. Zhong, S.H.; Seltmann, R.; Qu, H.; Song, Y. Characterization of the zircon Ce anomaly for estimation of oxidation state of magmas: A revised Ce/Ce* method. *Mineral. Charact. Petrol.* **2019**, *113*, 755–763. [CrossRef]

44. Delgado, J.; Soler, A. Ilvaite stability in skarns from the northern contact of the Maladeta batholith, Central Pyrenees (Spain). *Eur. J. Mineral.* **2010**, *22*, 363–380.

45. Yu, M. Metallogenic Mechanism of the Galinge Polymetallic Iron Skarn Deposit, QimanTagh Mountains, Qinghai Province. Ph.D. Thesis, Peking University, Beijing, China, 2017.

46. Dziggel, A.; Wul, K.; Kolb, J.; Meyer, F.M.; Lahaye, Y. Significance of oscillatory and bell-shaped growth zoning in hydrothermal garnet: Evidence from the Navachab gold deposit, Namibia. *Chem. Geol.* **2009**, *262*, 262–276. [CrossRef]

47. Inguaggiato, C.; Censi, P.; Zuddas, P.; Londoño, J.M.; Chacón, Z.; Alzate, D.; Brusca, L.; D'Alessandro, W. Geochemistry of REE, Zr and Hf in a wide range of pH and water composition: The Nevado del Ruiz volcano-hydrothermal system (Colombia). *Chem. Geol.* **2015**, *417*, 125–133. [CrossRef]

48. Michard, A. Rare earth element systematics in hydrothermal fluids. *Geochim. Cosmochim. Acta.* **1989**, *53*, 745–750. [CrossRef]

49. Peng, H.J.; Zhang, C.Q.; Mao, J.W.; Santosh, M.; Zhou, Y.M.; Houe, L. Garnets in porphyry–skarn systems: A LA-ICP-MS, fluid inclusion, and stable isotope study of garnets from the Hongniu–Hongshan copper deposit, Zhongdian area, NW Yunnan Province, China. *J. Asian Earth Sci.* **2015**, *103*, 229–251. [CrossRef]

50. Feng, C.Y.; Zhao, Y.M.; Li, D.X.; Liu, J.N.; Xiao, Y.; Li, G.C.; Ma, S.C. Skarn typesand mineralogical characteristics of the Fe-Cu-polymetallic Skarn deposits in the Qimantage area, western Qinghai Province. *Acta. Geol. Sin.* **2011**, *85*, 1108–1115. (In Chinese with English abstract)

51. Zhao, Y.M.; Lin, W.W.; Bi, C.S.; Li, D.X.; Jiang, C.J. *Skarn Deposits in China*; Beijing; Geological Publishing House: Beijing, China, 1990; pp. 1–354. (In Chinese with English abstract)

52. Zhao, Y.M.; Feng, C.Y.; Li, D.X.; Liu, J.N.; Xiao, Y.; Yu, M.; Ma, S.C. Metallogenic setting and mineralization-alteration characteristics of major skarn Fe-polymetallic deposits in Qimantag area, western Qinghai Province. *Miner. Depos.* **2013**, *32*, 1–19. (In Chinese with English abstract)

53. Li, D.X.; Feng, C.Y.; Zhao, Y.M.; Li, Z.F.; Liu, J.N.; Xiao, Y. Mineralization and alteration types and skarn minerology of Kaerqueka copper polymetallic deposit in Qinghai Province. *J. Jilin Univ.* **2011**, *41*, 1818–1830. (In Chinese with English abstract)

54. Liu, J.N.; Feng, C.Y.; Zhao, Y.M.; Li, D.X.; Xiao, Y.; Zhou, J.H.; Ma, Y.S. Characteristics of intrusiverock, metasomatites, mineralization and alteration in Yemaquan skarn Fe-Zn-polymetallic deposit, Qinghai Province. *Miner. Depos.* **2013**, *32*, 77–93. (In Chinese with English abstract)

55. Ma, S.C.; Feng, C.Y.; Zhang, D.J.; Shu, X.F.; Liu, J.N.; Du, S.J. Alteration and mineralization zoning of Hutouya polymetallic deposit in Qimantage area, Qinghai Province. *Miner. Depos.* **2013**, *32*, 109–121. (In Chinese with English abstract)

56. Xiao, Y.; Feng, C.Y.; Liu, J.N.; Yu, M.; Zhou, J.H.; Li, D.X.; Zhao, Y.M. LA-MC-ICPMS zircon U-Pb dating and sulfur isotope characteristics of Kendekeke Fe-polymetallic deposit, Qinghai Province. *Miner. Depos.* **2013**, *32*, 177–186. (In Chinese with English abstract)

57. Wang, S.; Feng, C.Y.; Li, S.J.; Jiang, J.H.; Li, D.S.; Su, B.S. Zircon SHRIMP U-Pb dating of granodiorite in the Kaerqueka polymetallic ore deposit, Qimantage Mountain, Qinghai Province, and its geological implications. *Geol. China* **2009**, *36*, 74–84. (In Chinese with English abstract)

58. Hu, H.; Li, J.W.; Lentz, D.; Ren, Z.; Zhao, X.F.; Deng, X.D.; Hall, D. Dissolution -reprecipitation process of magnetite from the Chengchao iron deposit: Insights into ore genesis and implication for in-situ chemical analysis of magnetite. *Ore Geol. Rev.* **2014**, *57*, 393–405. [CrossRef]

59. Sun, Z.Y.; Wang, J.B.; Wang, Y.W.; Long, L.L. Geochemical Characteristics of Mineral Assemblages from the Yamansu Iron Deposit, NW China, and Their Metallogenic Implications. *Minerals* **2020**, *39*, 39. [CrossRef]

60. Zhang, Y.; Shao, Y.J.; Zhang, R.Q.; Li, D.F.; Liu, Z.F.; Chen, H.Y. Dating Ore Deposit Using Garnet U–Pb Geochronology: Example from the Xinqiao Cu–S–Fe–Au Deposit, Eastern China. *Minerals* **2018**, *8*, 31. [CrossRef]

61. Kolb, J. The role of fluids in partitioning brittle deformation and ductile creep in auriferous shear zones between 500 and 700 °C. *Tectonophysics* **2008**, *446*, 1–15. [CrossRef]

62. Sun, Z.Y.; Wang, J.B.; Wang, Y.W.; Long, L.L.; Hu, Q.T.; Wang, M.L.; Li, D.D.; Xie, H.J. Two generations of garnets and their relevance for the hydrothermal fluid evolution of the Hongyuntan deposit, NW China. *Ore Geol. Rev.* **2022**, *122*, 103513. [CrossRef]